Supplementary File:

Table S1: Descriptive analysis of particle size distribution and modes during the study period and different seasons.

	Geom. Mean (nm)	Nucleation (cm^{-3})	Aitken (cm^{-3})	Accumulation (cm^{-3})	Total (cm^{-3})
Entire Study Period					
mean	6.48e+01	7.28e+03	1.77e+04	9.82e+03	3.48e+04
std	2.20e+01	5.81e+03	1.24e+04	7.05e+03	1.99e+04
min	2.01e+01	7.61e+01	1.36e+03	4.84e+02	2.41e+03
25%	4.83e+01	2.88e+03	8.74e+03	4.83e+03	2.06e+04
50%	6.26e+01	5.74e+03	1.43e+04	8.12e+03	3.05e+04
75%	7.91e+01	1.01e+04	2.28e+04	1.27e+04	4.38e+04
max	1.66e+02	6.54e+04	9.02e+04	6.33e+04	1.43e+05
Winter					
mean	7.70e+01	5.64e+03	2.13e+04	1.42e+04	4.11e+04
std	2.05e+01	5.56e+03	1.53e+04	8.82e+03	2.44e+04
min	2.56e+01	7.61e+01	2.70e+03	1.98e+03	6.50e+03
25%	6.24e+01	1.97e+03	1.05e+04	7.79e+03	2.35e+04
50%	7.62e+01	4.01e+03	1.60e+04	1.13e+04	3.42e+04
75%	9.02e+01	7.27e+03	2.71e+04	1.85e+04	5.27e+04
max	1.43e+02	6.54e+04	9.02e+04	6.33e+04	1.43e+05
Spring					
mean	5.46e+01	1.01e+04	1.80e+04	7.65e+03	3.57e+04
std	1.90e+01	6.59e+03	1.07e+04	4.20e+03	1.62e+04
min	2.01e+01	3.69e+02	2.07e+03	1.13e+03	4.86e+03
25%	3.91e+01	5.14e+03	1.01e+04	4.52e+03	2.42e+04
50%	5.08e+01	8.82e+03	1.55e+04	6.69e+03	3.32e+04
75%	6.69e+01	1.40e+04	2.31e+04	1.03e+04	4.40e+04
max	1.19e+02	4.34e+04	5.95e+04	2.50e+04	9.36e+04
Summer					
mean	5.66e+01	6.89e+03	1.28e+04	5.62e+03	2.53e+04
std	1.92e+01	5.21e+03	8.58e+03	3.53e+03	1.37e+04
min	2.11e+01	1.94e+02	1.36e+03	4.84e+02	2.41e+03
25%	4.20e+01	2.77e+03	6.59e+03	3.05e+03	1.50e+04
50%	5.42e+01	5.47e+03	1.00e+04	4.73e+03	2.27e+04
75%	6.97e+01	9.83e+03	1.64e+04	7.45e+03	3.29e+04
max	1.30e+02	3.01e+04	4.79e+04	1.99e+04	8.54e+04
Post Monsoon					
mean	6.69e+01	8.21e+03	1.95e+04	1.15e+04	3.92e+04
std	2.06e+01	5.25e+03	1.13e+04	4.84e+03	1.66e+04
min	2.85e+01	4.39e+02	2.20e+03	2.43e+03	6.60e+03
25%	5.28e+01	4.39e+03	1.06e+04	7.76e+03	2.68e+04
50%	6.23e+01	7.19e+03	1.68e+04	1.14e+04	3.67e+04
75%	7.72e+01	1.10e+04	2.62e+04	1.47e+04	4.89e+04
max	1.66e+02	3.26e+04	7.36e+04	3.88e+04	1.11e+05

4

5

6

7

8

9

10

11

12

13

14

15

16

Table S2: Calibration values applied to the dataset.

Species	RIE	RF
Ammonium	4.64	3.36 E-11
Chloride	0.57	
Nitrate	1.05	
Sulphate	0.89	
Organics	1.4	

Table S3: Comparison of $PM_{2.5}$ (or PM_1) concentration ranges and averages across different studies in Delhi.

S. No.	Average concentration (µg/m³)	PM type	Period of Study	Data Source	References
1	125 ± 86 (Entire study period, 15 years)	$PM_{2.5}$	2007-2021	CPCB, DPCC, and IMD	Chetna et al. (2022)[1]
	154 ± 51 (Highest Annual average, 2009)				
	99 ± 81 (Lowest Annual average, 2020)				
2	Annual mean in excess of 100 for each year	$PM_{2.5}$	2013-2019	US embassy in New Delhi	Li et al. (2019)[2]
3	167.6	$PM_{2.5}$	Winter (Dec 2013 -Jan 2014) and Summer (June 2014)	Offline filter-based	Pant et al. (2015)[3]
	12-hourly average range (3-3 - 424.9)				
	108.75 (Excluding Post Monsoon period)	NR-PM_1 + BC	Jan 2017 to March 2018	ACSM and Aethalometer	Gani et al. (2019)[4]
4	Daily average range (13 and above 400)				
5	140	$PM_{2.5}$	2017	DPCC RK Puram	Gani et al. (2019)[4]
6	125	$PM_{2.5}$	2022 (Excluding the Monsoon period as in our study)	DPCC, RK Puram and CPCB, Sri Aurobindo Marg	CPCB
	Hourly Range (5.25 - 920)				

18

Table S4: Condensation sink (CS) thresholds for new particle formation (NPF) observed in various global
19
locations, highlighting differences between urban, semi-urban, remote, and background regions. The table
20
includes a comparison of CS thresholds across different environments, showing how regional pollution levels
21
and aerosol concentrations influence the threshold for NPF.
22

S. No.	CS Threshold (s⁻¹)	Region	Region Type	Reference
1	0.01	Boreal forest in Hyytiälä, Finland.	Remote	Dada et al. (2017)[5]
2	0.039	Beijing, China	Urban	Ying Zhou et al. (2021)[6]
3	0.02	Po Valley, Italy	Urban	Cia et al. (2024)[7]
4	0.06	Beijing, China	Urban	Du et al. (2022)[8]
5	0.001 to 0.002	6 Arctic regions	Remote	Brean et al. (2023)[9]
6	0.002	Southeastern Tibetan Plateau	Remote	Lai et al. (2024)[10]
7	0.007	Delhi, India	Urban	Monkkonen et al. (2005)[11]
8	0.1	Shangai, China	Urban	Xiao et al. (2015)[12]
9	0.0046	Eagle Lake, British Columbia, Canada	Remote	Andreae et al. (2022)[13]
10	0.03	Pune, India	Semi-urban	Kanawade et al. (2014)[14]
11	0.06	Kanpur, India	Semi-urban	Kanawade et al. (2014)[14]
12	0.0058	Western Himalaya, India	Mountain background	Sebastian et al. (2021)[15]
13	0.002	Helsinki, Finland	Urban	Hussein et al. (2008)[16]
14	0.003	Leece, Italy	Urban	Dinoi et al. (2021)[17]

23

24

25

26

27

28

29

30

31

32

33

34

S1. Sampling Site

The aerosol sampling occurred inside the Indian Institute of Technology (IIT), Delhi campus, situated at coordinates 28.5457° N and 77.1928° E, with an elevation of 230 meters above sea level. The campus is in South Delhi and is surrounded by residential, educational, and commercial buildings, representing the urban Delhi area (Figure S1). The nearest local emission source is an arterial road approximately 150 meters from the sampling site.
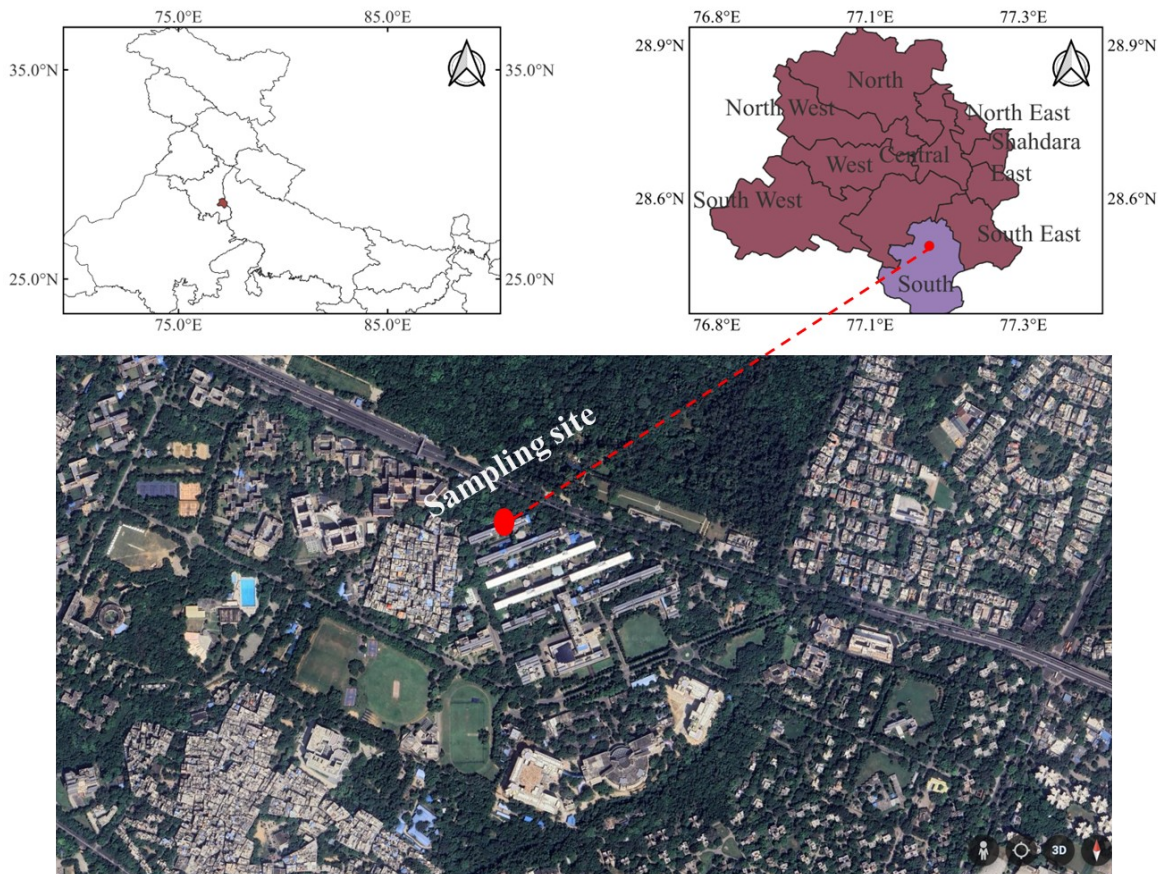

Figure S1: Location of the sampling site.

S2. Instrumentation Operation and calibration

A PM$_{2.5}$ cyclone was installed before the sampling inlet to remove coarse particles larger than 2.5 μm. The PM + Cyclone model used was URG-2000-30ED. An external pump drew ambient air into the container at a flow rate of 3 L/min, with approximately 0.1 L/min of the drawn air being sampled into the ACSM. The particle residence time in the sampling tube was about 5 seconds. Aerosol particles were dried using a Nafion dryer before being sampled into the ACSM. Prior to the campaign, the ACSM was calibrated with pure ammonium nitrate and ammonium sulphate particles following

50 standard protocols. The sampling line was placed on a rooftop (~15 m above ground level), and the

51 instruments were located inside a temperature and humidity-controlled room on the topmost floor.

52 Conditions inside the building were maintained at temperatures below 26°C and relative humidity

53 below 40%.

54 A ¼ inch (outside diameter) stainless steel tube with a flow rate of 1.7 lpm was used to draw an

55 ambient air sample inside the well-maintained and temperature-controlled room, of which 0.1 lpm

56 was subsampled into the ACSM. At the beginning of the sample intake, a URG cyclone with a cut-

57 off size of 2.5 μm was fitted to remove coarser particles. An automatic aerosol Nafion dryer was used

58 at the ACSM inlet to keep the relative humidity of the sampled air below 40 %. The sampling inlet

59 was installed on the roof directly above the instrument, giving the residence time of around 5 s in the

60 sampling line. ACSM was operated at a 10-time resolution during both winters, then averaged to an

61 hourly interval. The $PM_{2.5}$-Q-ACSM uses a capture vaporizer (CV) to detect $PM_{2.5,}$ and the collection

62 efficiency (CE) taken is 1[18].

63 The ionization efficiency (IE) of NO_3 and relative ionization efficiencies (RIE) of NH_4 and SO_4 were

64 estimated following the procedure suggested by Crenn et al. (2015)[19]. A differential mobility analyser

65 (DMA) was used to select monodisperse 300 nm particles of NH_4NO_3 and $(NH_4)_2SO_4$ size within a

66 wide range of concentrations. The particles were sampled into a condensation particle counter (CPC)

67 and the ACSM.

68 Using the mass computed using the known particle size and the number concentrations from CPC, t

69 he response factors of ACSM were compared to determine IE. The calibration values are given in

70 table S2.

71 0.28 lpm of the ambient air was drawn into the SMPS following the drying through Nafion dryer.

72 Further days hours with less than 75 % of the data were removed from the analysis. Measurements
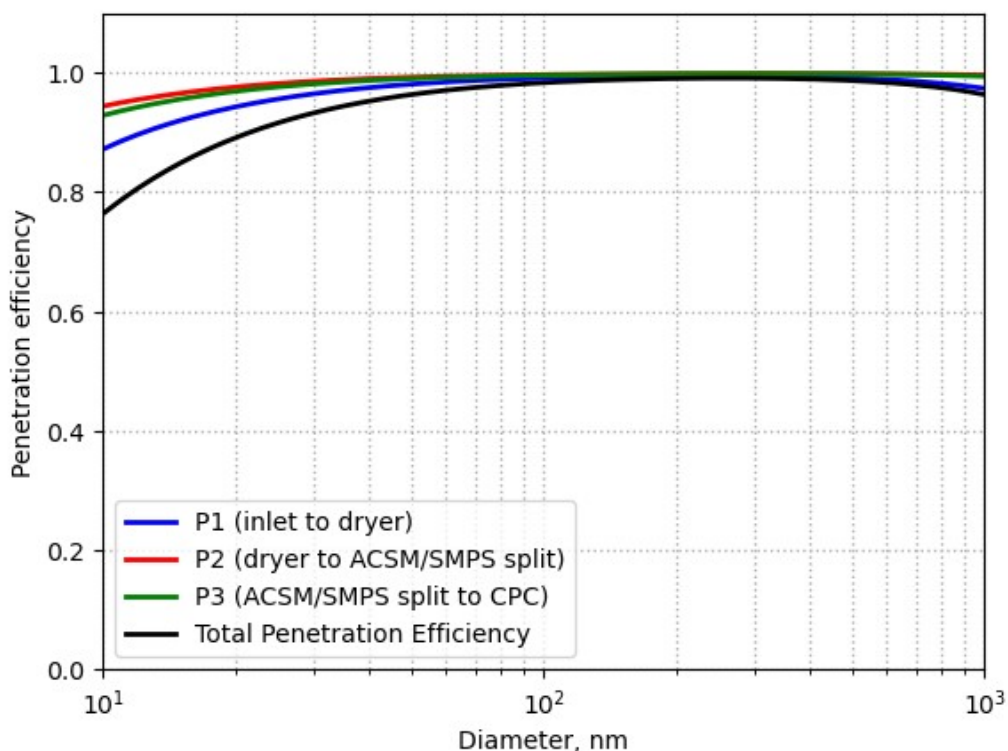
Figure S2: Transmission efficiency of the sampling line, computed for both diffusion [21] and settling [20] losses.

73 during rainy days were not considered for analysis. The diffusion and settling losses of particles in

74 sampling lines were estimated using the calculations. [20,21] We adjusted the measured PNSDs to

75 account for the losses in transmission efficiency (Figure S2). Subsequently, we determined the total

76 and number of concentrations for each size mode. Additionally, we calculated the median diameter

77 using the updated PNSDs. The quality check of data included cleaning the data, removing outliers,

78 and discarding abnormal datasets.

79 **S3. Density and mass closure**

80 We estimated the mass concentration of PM1 from the PNSD measurements of SMPS using a constant

81 density. In this study, the density of $PM_{2.5}$, including the non-refractory portion of aerosols and black

82 carbon (BC), was estimated to be approximately 1.6 g/cm³. Previous studies in Asia [22–24] reported aerosol

83 densities between 1.3 and 1.6 g/cm³, while [25] used a density of 1.7 g/cm³ for aerosol mass calculations

84 in Delhi. In this study we have used a density of 1.6 g/cm³. This density provides a good mass closure,

85 as evident from the plot of $PM_{2.5}$ vs. PM_1 (Figure S3). $PM_{2.5}$ and PM_1 are in good agreement. There are

86 some points when PM_1 was greater than $PM_{2.5}$ however we have removed them from our analysis.
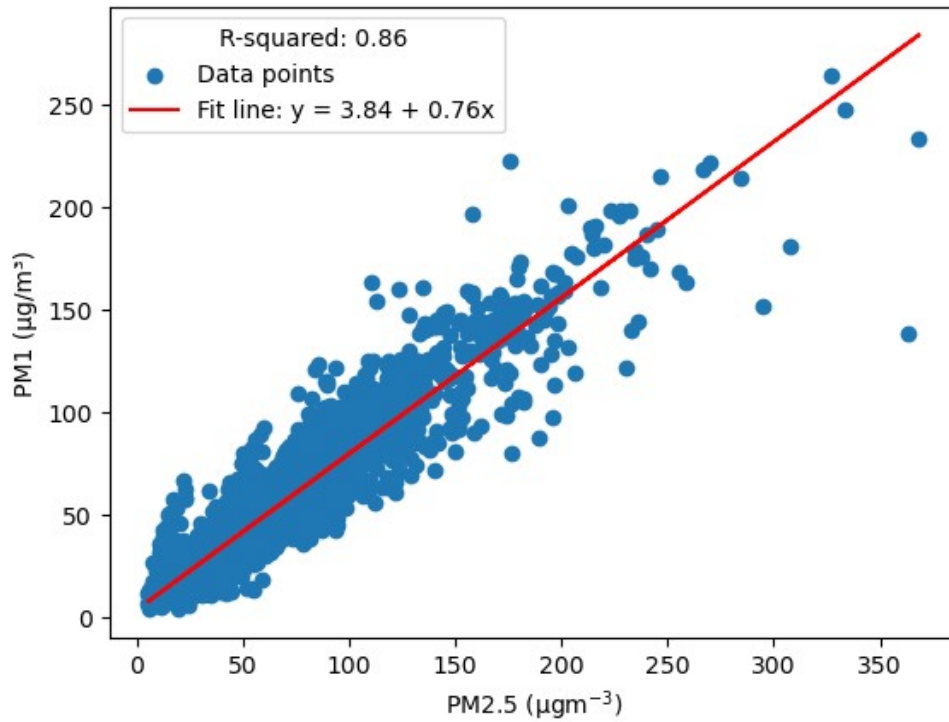
Figure S3: Scatter plot between PM$_1$ (calculated using SMPS PNSD assuming a density of 1.6 g/cc) and PM$_{2.5}$ (NR-PM$_{2.5}$ +BC).

87

88

89

90

91

S4. ALWC Measurement

The ISORROPIA II model ignores curvature and surface tension effects and assumes that aerosol water intake does not affect ambient water vapor pressure, resulting in aerosol water activity (a_w) equalling RH. The ZSR mixing rule [26] is used to calculate ALWC.

$$ALWC = \sum \frac{M_i}{m_{oi}(a_w)} \tag{S1}$$

where ALWC denotes the condensed aerosol water mass concentration (kg m^{-3} air), M_i denotes the concentration of ith component (mol m^{-3} air), and m_{oi} (a_w) is the molality of an aqueous binary solution of the ith electrolyte with the same a_w (i.e., relative humidity) as the multicomponent solution.

For organics, the following equation was used to calculate the contribution to ALWC:

$$W_o = \frac{m_{org}\rho_w}{\rho_{org}} \frac{\kappa_{org}}{(1/RH - 1)} \tag{S2}$$

Where m_{org} denotes the organics mass concentration as measured by ACSM, ρ_w (1 g/cm^3) and ρ_{org} (1.5 g/cm^3) represent the densities of water and organics, respectively, and κ_{org} denotes the

104 hygroscopicity of organic aerosols taken as 0.1. The uncertainties related to hygroscopicity of
105 organics have been discussed in our other paper. [27]

106 **S5. Source apportionment of analysis of organics using positive matrix factorization (PMF)**
107 Source apportionment (SA) through a positive matrix factorization (PMF) was performed on the mass
108 spectra of the OA aerosol in each season individually to gain insights into the effect sources and
109 atmospheric processes on OA. SA of OA aerosols was deconvoluted into five factors in the summer
110 and winter seasons, while 3-factor solution was identified in the post monsoon season. The factors
111 were resolved and identified based on distinct spectral signals in specific factors (Fig. S4). Also, this
112 spectral factor was correlated with the factor profile of the AMS Spectral Database, which is available
113 at http://cires.colorado.edu/jimenez-group/AMSsd/).
114 The factors resolved in the current analysis are HOA, BBOA, LVOOA1, LVOOA2, and SVOOA in
115 summer and winter, while in post monsoon, it is deconvoluted into LVOOA1, LVOOA2, and POA.
116 The HOA factor profile is characterized by the distinct signals of primary alkyl fragments (CxHy
117 groups) at mz 27, 41, 43, 55, 57, 69 and 71. BBOA profile has distinct signals of mz 60 and mz 73,
118 which are linked to the anhydrous sugar signals. [28] SOA factors are characterized by the distinct
119 signals of the mz 43 and mz 44 ($C_2H_3O^+$ and CO_2^+). These SOA factors are surrogates for the
120 secondary aerosol formation in the summer and winter. Mass spectra profile factors in different
121 seasons and details regarding each factor's temporal and diel variation in different seasons are
122 discussed below (Figure S4).
123 The BBOA factor exhibited discernible marker peaks corresponding to biomass burning markers,
124 namely m/z 60, 73. The enhanced peaks observed at m/z 60 suggest the presence of Laevoglucosan.
125 Laevoglucosan is associated with $C_2H_4O_2^+$ (a fragment with a mass of 60) and is frequently
126 employed as a characteristic marker of biomass burning in ACMS-AMS-based studies. [29] The
127 biomass burning factor also contributed 65% of the m/z 73 anhydrous sugar signals, which are widely
128 recognized as reliable indicators of wood-related combustion processes.[28] Resolved HOA factor had
129 clear spectral markers of primary alkyl fragments like m/z's 41, 43, 55, and 57, which are identified
130 for the majors for this factor. The LVOOA1and LVOOA 2 mass spectra are distinguished by distinct
131 peaks at m/z 44 or CO_2^+, which are tracer fragments used to label the oxygenated organic aerosol
132 (OOA). [29] Both OOA-1 and OOA-FW mass spectra demonstrated a significant correlation with low
133 volatile oxygenated organic aerosol (LVOOA) profiles (Pearson R = 0.93, 0.94 for OOA-1 and OOA-
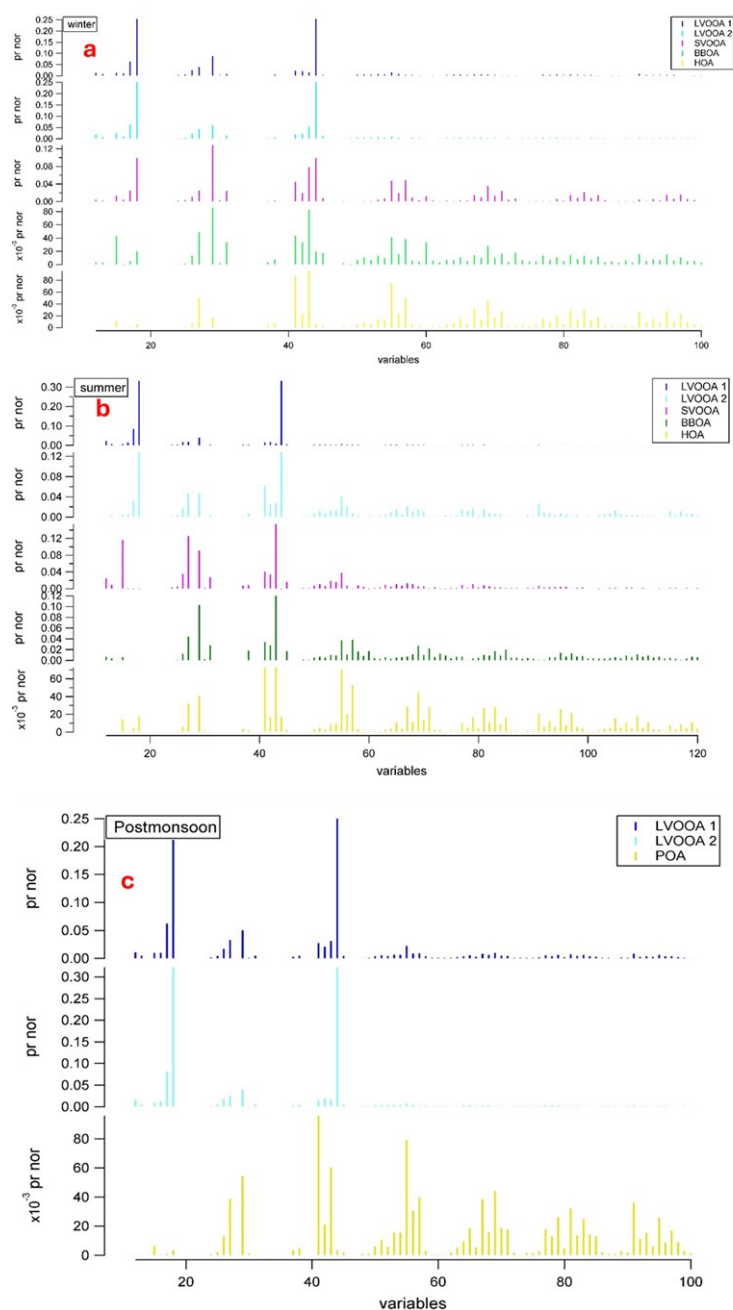134 2, respectively), consistent with standard profiles. [30]

Figure S4: Factor profiles of resolved organic aerosol factors during different seasons.

S6. NPF Identification

In addition to these two features, Delhi being a polluted city with continuous influence of traffic and other primary emissions, we also used we plotted temporal variation of primary species, such as black carbon, NOx, and CO, to rule out the primary emissions as the out the source of new mode of particles. [31] We also looked at the time variations of different modes of PNC, with a simultaneous increase in the concentration of all modes indicating a change in meteorological conditions or emissions. Furthermore, if the particle growth rates in an NPF event can be accurately predicted from the temporal evolution of PNSDs, it is categorised as a 'Type I' event, otherwise as Type II event. Figure

143 S5 (a -d): Diel variation of trace gas concentrations and meteorological conditions. NPF events were
144 classified based on the PNSD in which the appearance of fresh particles in the nucleation mode size
145 ranges (<25 nm) showing signs of growth independent of the meteorological conditions during that
146 day. Plots of trace gases, mode PNCs and meteorological conditions are given in Figure S5 and S6.
147 Furthermore, we used the diel variations of BC to validate the secondary origin of nucleation mode
148 particles, as BC serves as an excellent proxy for primary emissions [32,33]. The lack of correlation
149 between the peaks in BC and the timing of nucleation events further supports the secondary nature of
150 these particles. The diel patterns of BC observed during the selected NPF events, as shown in Figure
151 S7, illustrate that the nucleation events occurred independently of the primary emissions typically
152 reflected in BC concentrations. This highlights the role of secondary processes in the formation of
153 nucleation mode particles.
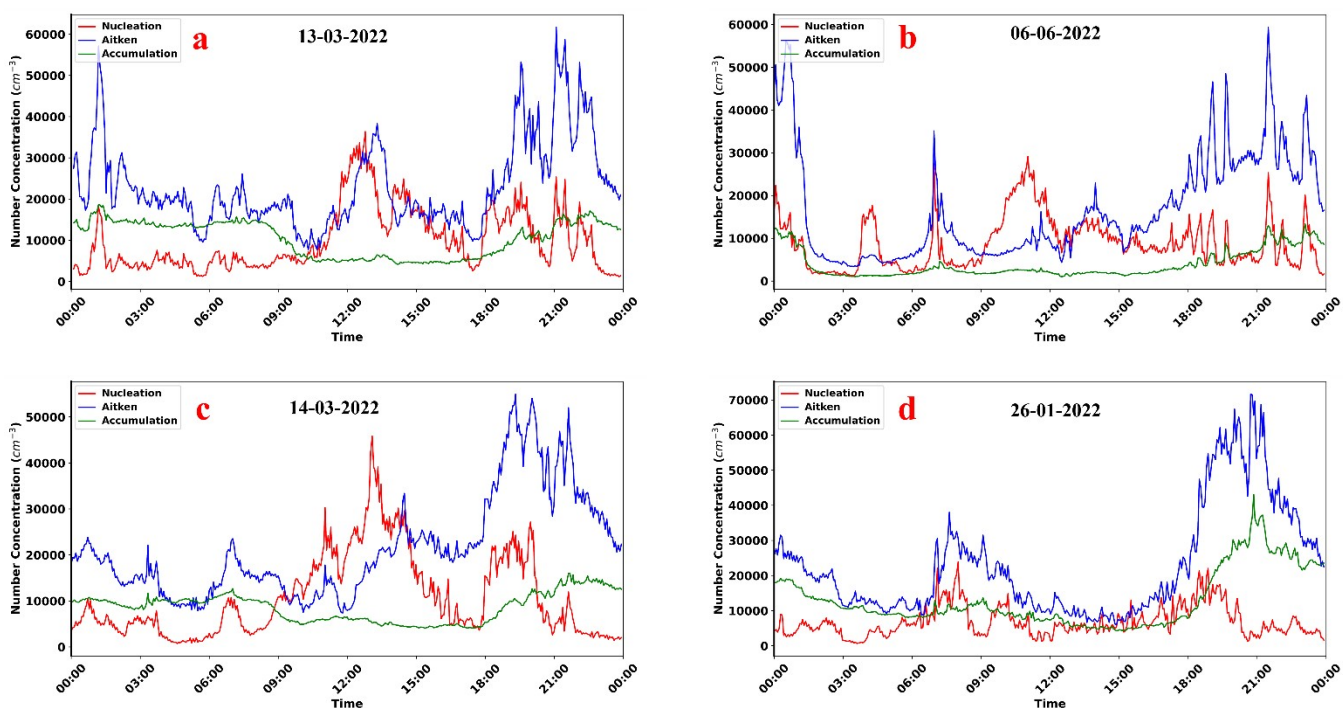
Figure S5: Diurnal variation of PN concentrations of nucleation, Aitken, and accumulation modes. As evident from the first three plots (a, b and c, number concentration of nucleation mode starts shows bursts during daytime on NPF events. In last plot (d), no burst of nucleation is observed during daytime, hence it's a non-NPF event.

154

155

156

157

158

159

160
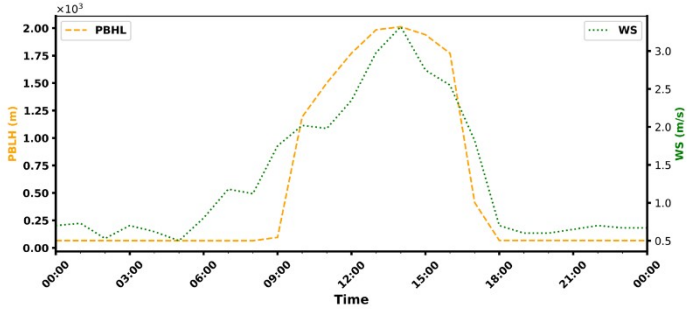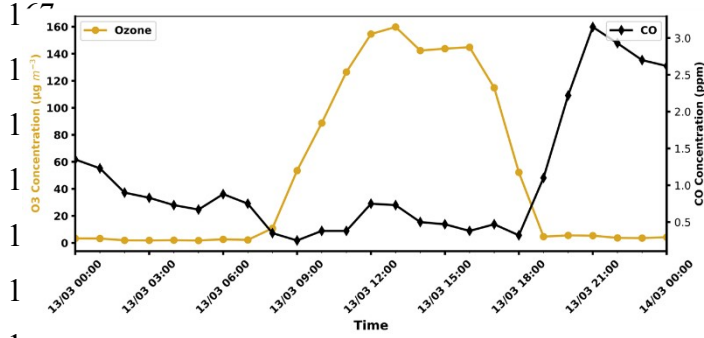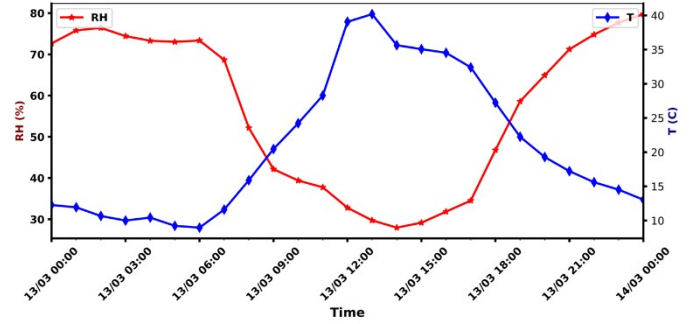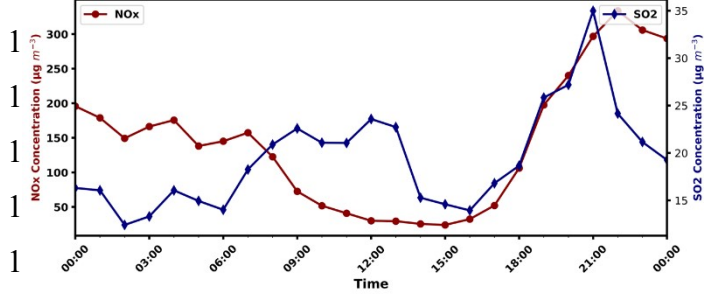
a

13-03-2022

173

174

b

14-03-2022

187

188

189
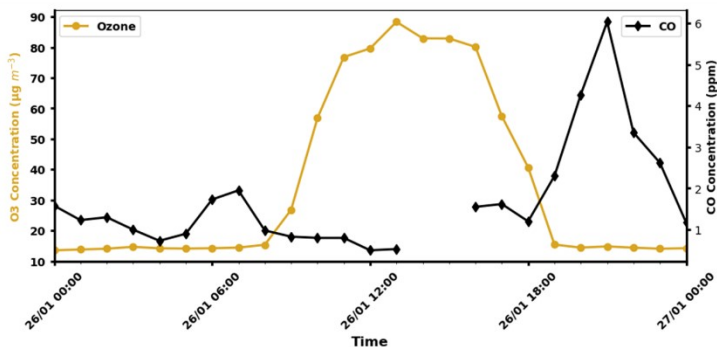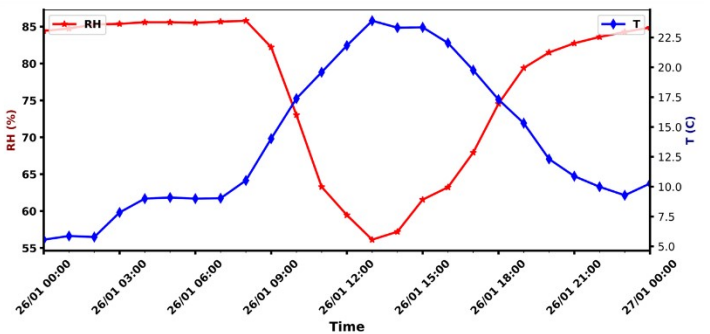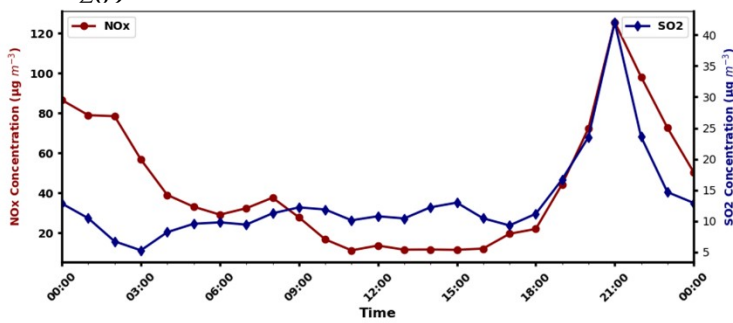
190
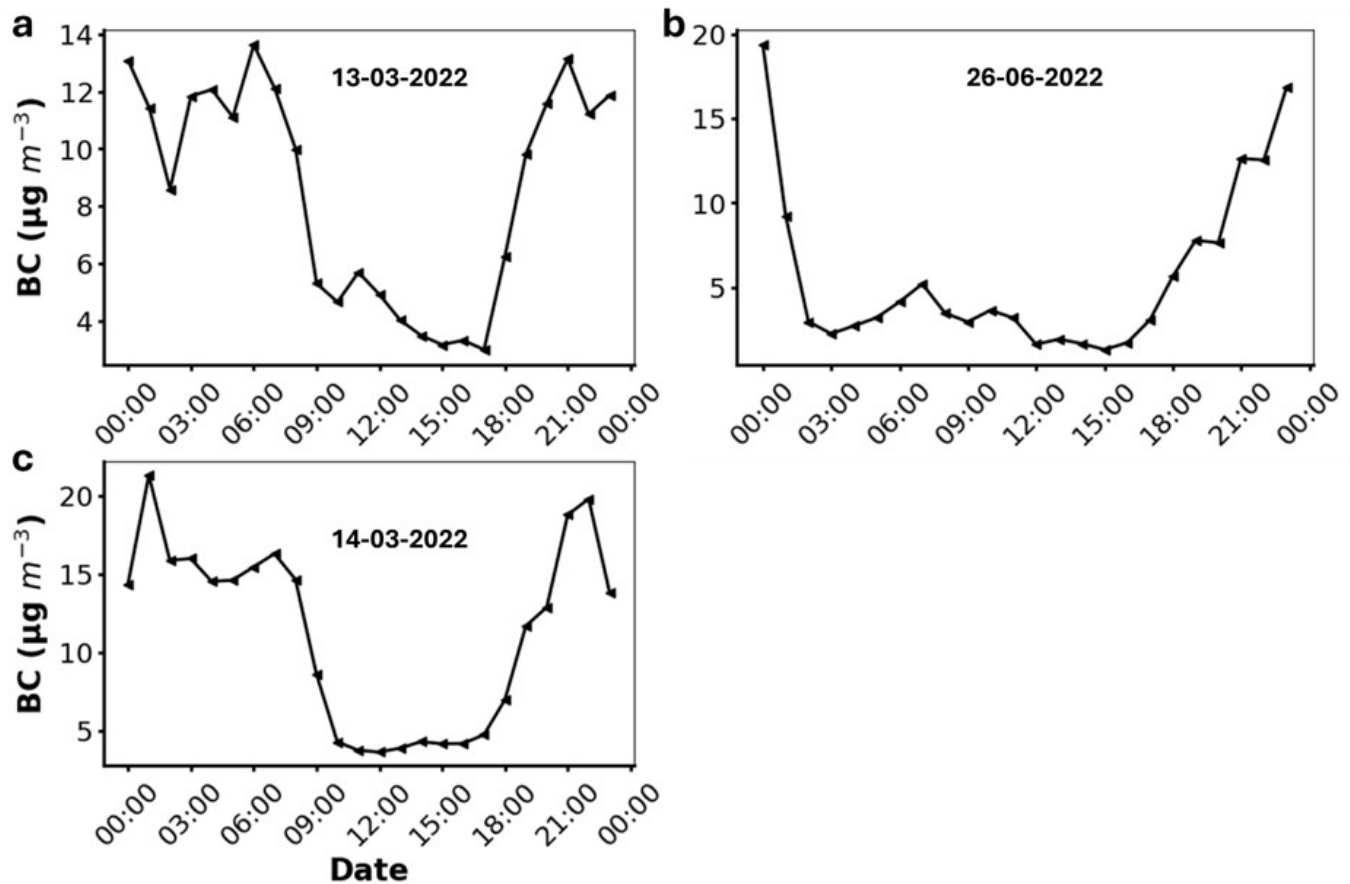
191

192
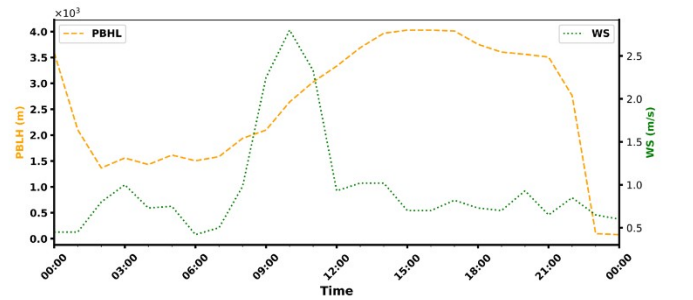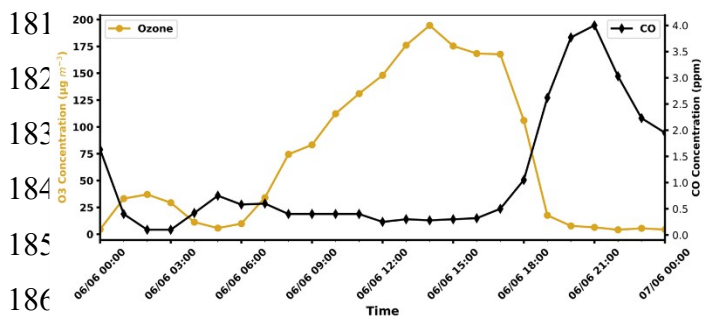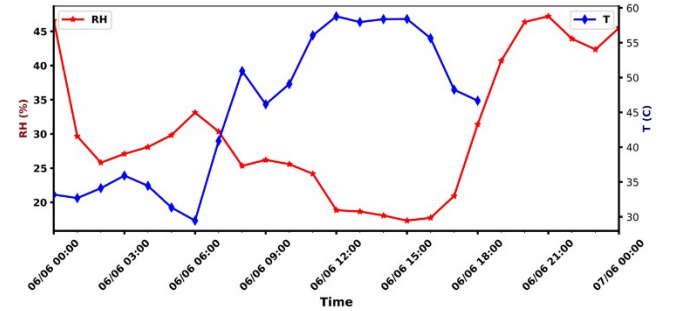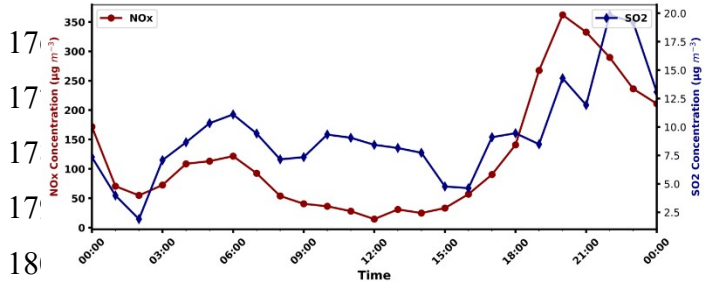
06-06-2022
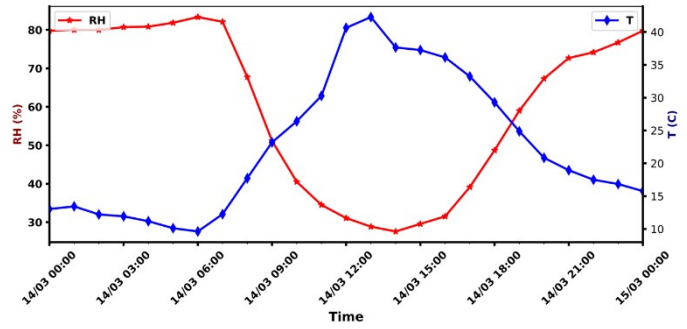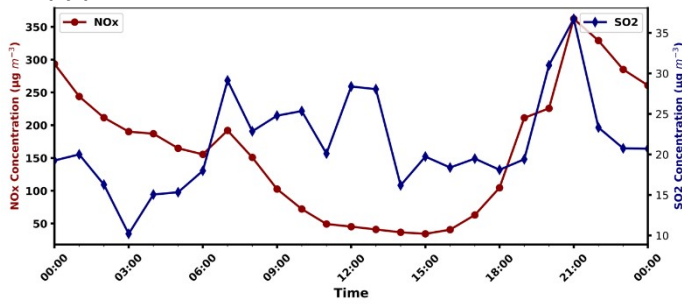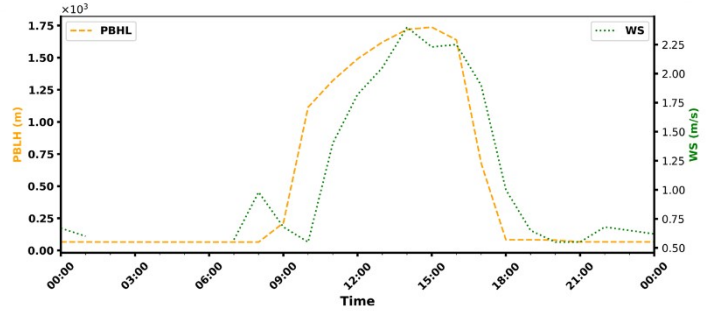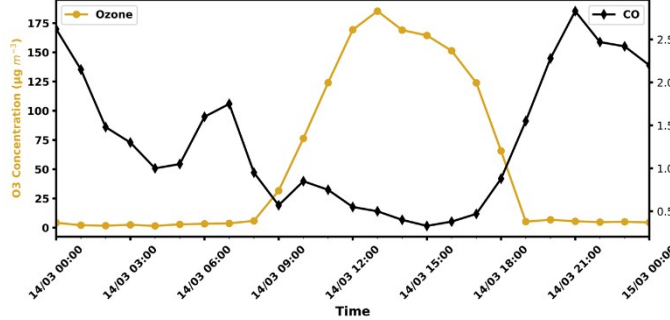
26-01-2022

Figure S6 (a -d): Diurnal variation of trace gas concentrations and meteorological conditions. NPF events were classified based on the PNSD in which the appearance of fresh particles in the nucleation mode size ranges (<25 nm) showing signs of growth independent of the meteorological conditions during that day.

219

Figure S7: Diel variation of Black Carbon (BC) concentrations on selected days. The absence
of significant daytime peaks in BC concentrations, particularly between 9:00 AM and 6:00 PM,
suggests limited influence from secondary formation during the day and reinforces the
identification of BC as a proxy for primary emission sources, largely driven by anthropogenic
activities during nighttime and early morning hours. This pattern closely mirrors the diel profile
of CO, further confirming the primary nature of the observed nucleation events.

226

S7. Apparent Formation rate (J_{10})

The apparent formation rate of 10 nm particles (J_{10}) was calculated using the following equation[34]:

$$J_{10} = \frac{dN_{10-25}}{dt} + CoagS \cdot N_{10-25} + \frac{GR_{10-25}}{15} \cdot N_{10-25} \qquad \text{S3}$$

The right hand side of the Eq. (S3) includes the measured change of the particle concentration per
time interval (first term), the loss by coagulation scavenging (second term) and the growth out of the
specific size range at 25 nm (third term). Where, N_{10-25} is the particle concentration in the 10-25 nm
range, representing nucleation mode. The GR is the growth rate of nucleation mode particles.

CoagS is the coagulation sink for particles of diameter D_{pi} (representative size of nucleation mode;
15 nm) and is derived from the size distribution.[35]

$$\text{CoagS}_i = \sum_j K_{ij} N_j$$

236   S4

237 Here N_j is the particle number concentration of the j th size bin, and $K_{ij}(cm^3 No^{-1} s^{-1})$ is the

238 coagulation coefficient between particles of the j th bin (diameter D_{pj}) and i th bin. [36]

$$K_{ij} = 2\pi(D_i + D_j)(D_{pi} + D_{pj})\left(\frac{D_{pi} + D_{pj}}{D_{pi} + D_{pj} + 2(g_i^2 + g_j^2)^{1/2}} + \frac{8(D_i + D_j)}{(\bar{c}_i^2 + \bar{c}_j^2)^{1/2}(D_{pi} + D_{pj})}\right)^{-1}$$

239   S5

240 where

$$\bar{c}_i = \left(\frac{8kT}{\pi m_i}\right)^{1/2}$$

$$l_i = \frac{8D_i}{\pi \bar{c}_i}$$

$$g_i = \frac{\sqrt{2}}{3D_{pi} l_i}\left[(D_{pi} + l_i)^3 - (D_{pi}^2 + l_i^2)^{3/2}\right] - D_{pi}$$

$$D_i = \frac{kTC_c}{3\pi\mu D_{pi}}$$

241

S8. H₂SO₄ estimation

243 Measuring sulfuric acid gases in the lower troposphere is challenging due to their generally low

244 ambient concentrations, typically ranging from 10^6 to 10^7 molecules/cm³. Various methods have been

245 proposed to estimate ambient sulfuric acid concentrations based on observations such as SO_2.

246 Previous studies [37–39] have suggested different approaches in this regard. For instance, Petäjä et al.

247 (2009)[39] introduced a linear method to approximate observed H_2SO_4 concentration in Hyytiälä,

248 southern Finland, while Lu et al. (20119) proposed a nonlinear method, presenting several proxies

249 for gaseous sulfuric acid concentration. Their study indicated that compared to the linear method, a

250 nonlinear relationship offers more accurate H_2SO_4 concentration estimates, particularly in Beijing.

251 Additionally, Mikkonen et al. (2011)[38] utilized another sulfuric acid nonlinear proxy based on long-

252 term observations in various locations. Dada et al (2020)[37] proxies for sulfuric acid (H_2SO_4)

253 concentrations were derived using measurements from four distinct locations: a boreal forest in

254 Hyytiälä, Finland; a rural Mediterranean site in Agia Marina, Cyprus; an urban area in Budapest,

255 Hungary; and a megacity in Beijing, China. These proxies were based on a combination of the

256 identified sources and sinks of H_2SO_4.

257 Despite their utility, these methods carry significant uncertainties, as few studies have explored their

258 accuracy across diverse locations, and none have been tested in complex environments like Delhi.

259 Despite these limitations, we have utilized the proxy provided by Dada et al. (2020)[37], which aligns
260 with measurements in Beijing, a city resembling Delhi regarding complexity and pollution levels.

261 **S9. Estimating Hygroscopic Growth Factors**

262 **Mass-Based Hygroscopic Growth Factor** $(G_f(mass\ based))$: The size-based hygroscopic

263 based growth factors (G_f) is defined as the the ratio of size of the wet aerosol particle to the

264 size of the aerosol particle particle at dry conditions (RH < 20%). It's a function of chemical

265 composition, RH and initial size of the dry particle. In our case we don't have the measurements

266 of hygroscopic growth factor, so employed a different approach to estimate the hygroscopic

267 growth factor. First we estimated ALWC using the ISSOROPIA II as discussed in section S4.

268 Then the mass based hygroscopic size growth factor was estimated as;

269
$$G_f(mass\ based) = \frac{PM_{2.5} + ALWC}{PM_{2.5}} \qquad \text{S6}$$

270 Where $PM_{2.5}$ is the dry aerosol mass at a particular RH condition and ALWC is the aerosol

271 liquid water content associated with $PM_{2.5}$ at those RH conditions.

272

273 **Size-Based Hygroscopic Growth Factor (G_f):**
274 Since particle density changes with water absorption, we need to account for this to estimate
275 the size-based hygroscopic growth factor. The size-based growth factor (G_f) is calculated
276 using:

277
$$G_f = \frac{Gf(mass-based)^{\frac{1}{3}} \times \rho_{dry} \times Gf(mass-based)}{\rho_{dry} + \rho_{water} \times (Gf(mass-based) - 1)} \qquad \text{S7}$$

278 Where ρ_{dry} is the density of dry $PM_{2.5}$ estimated as 1.6 g cm^{-3} based on the chemical

279 composition of $PM_{2.5}$ and ρ_{water} is the density of water taken as 1 g cm^{-3}.

280 This method estimates the hygroscopic growth of bulk $PM_{2.5}$, without considering size-specific

281 effects, using the chemical composition used was average daytime chemical composition of

282 $PM_{2.5}$.

283 The plot of hygroscopic growth vs RH is shown in the figure S18.
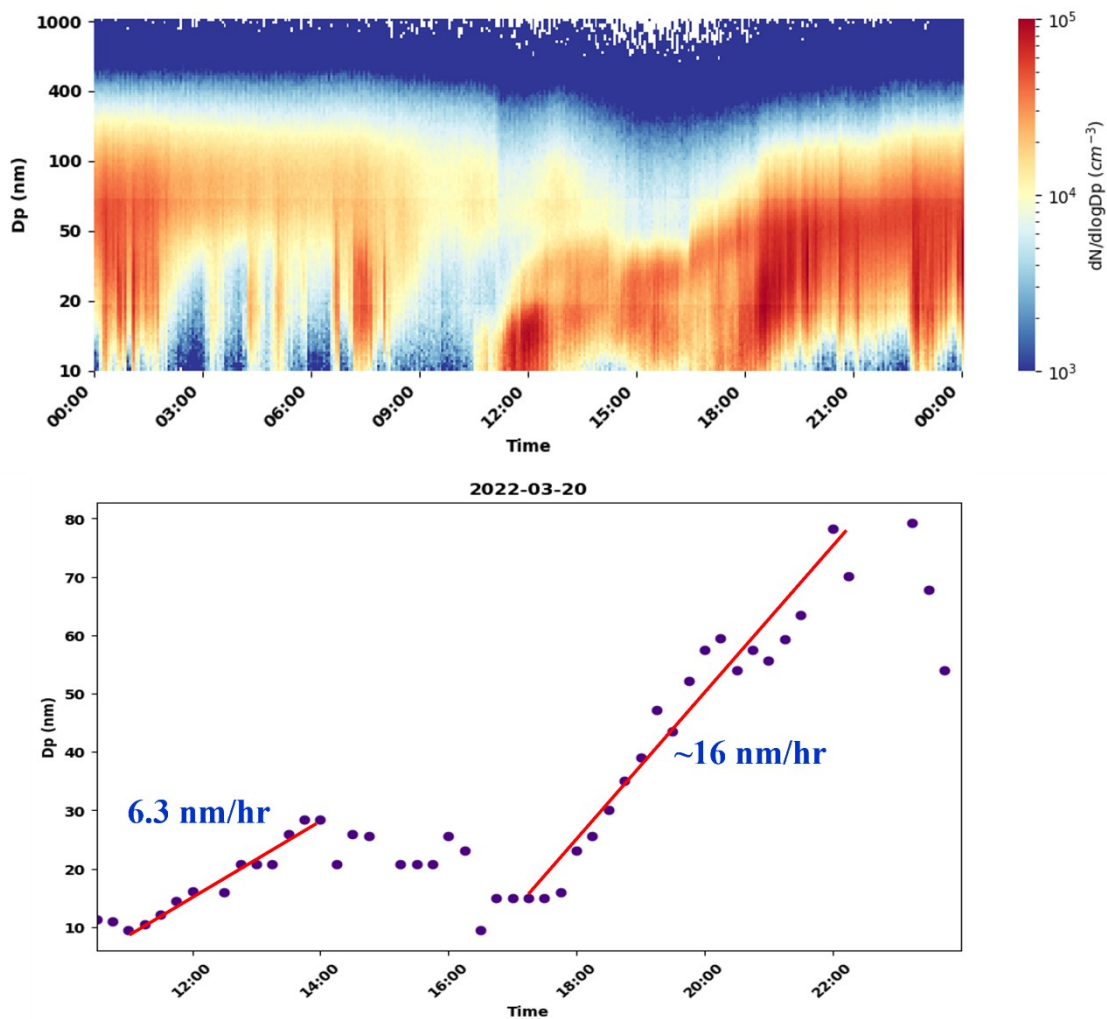
Figure S8: Daytime growth rate of nucleation mode particles calculated as the slope of a linear fit to the geometric mean of nucleation mode particles over time. The plot also shows a more rapid growth rate of particles observed during the evening hours, calculated similarly.

284

285

286

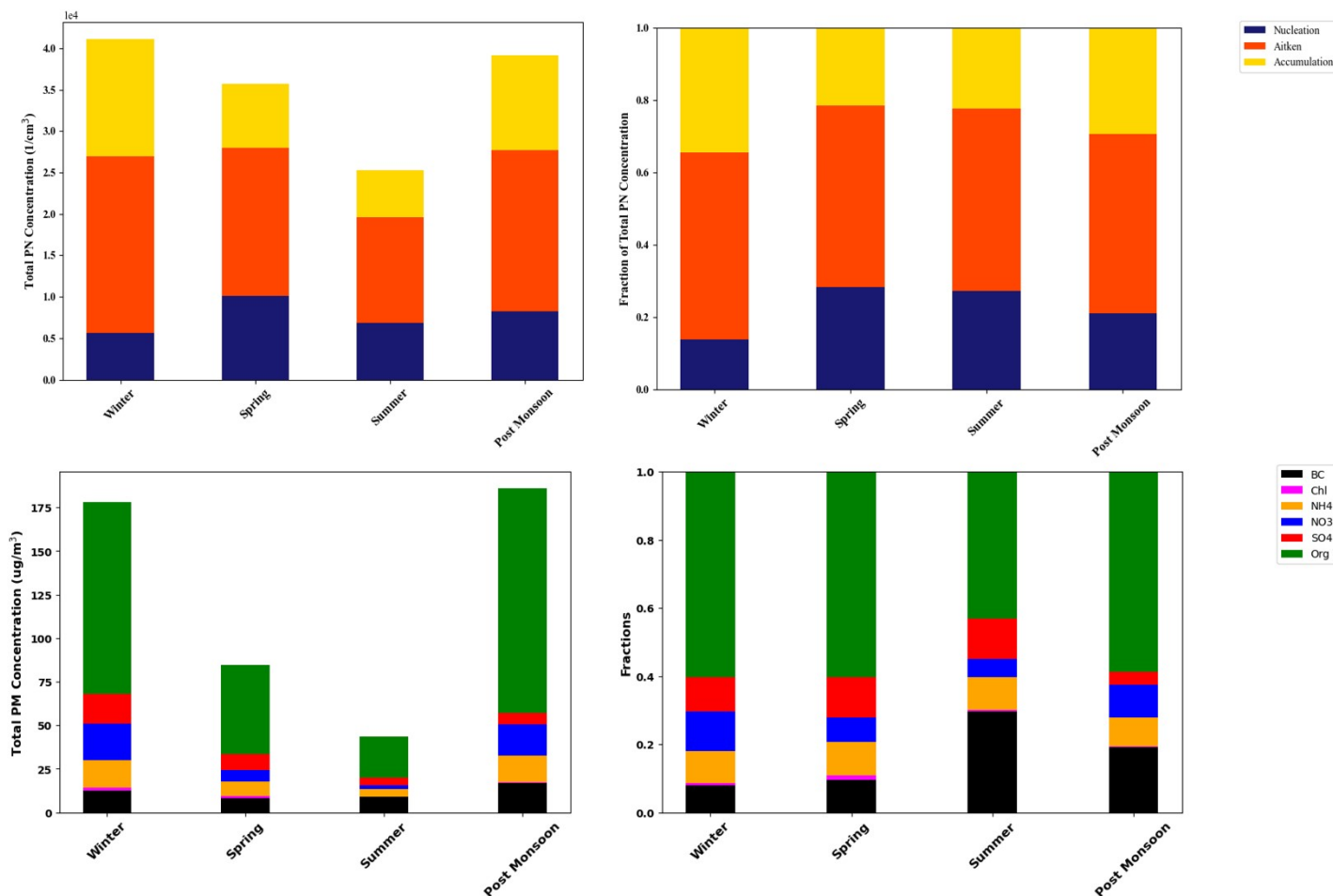287

288

289

290

291

292

293

294

295

Figure S9: Average particle number (PN) and PM₂.₅ levels for each season by mode and components, respectively.. The modes are based on scanning mobility particle sizer (SMPS) observations, namely nucleation (10-25 nm), Aitken (25-100 nm), and accumulation (100-1000 nm) modes. The PM₂.₅ species are organics (Org), chloride (Chl), ammonium (NH₄), nitrate (NO₃), sulfate (SO₄), and black carbon (BC).

Quantitative analysis of the plots reveals that PN levels follow the seasonal trends of PM₂.₅ levels but not in a directly proportional manner. During the winter season, PN levels reach approximately 40,000 cm⁻³ while PM₂.₅ levels are around 175 µg/m³. In the spring, PN levels decrease to about 30,000 cm⁻³ as PM₂.₅ levels drop to approximately 125 µg/m³. The summer season shows a further reduction in both, with PN levels around 20,000 cm⁻³ and PM₂.₅ levels at about 50 µg/m³. Post-monsoon, PN levels rise again to around 35,000 cm⁻³, similar to winter levels, whereas PM₂.₅ levels return to approximately 175 µg/m³.

However, the proportional changes are not consistent. For instance, while the PN levels in winter are about twice those in summer, the PM₂.₅ levels in winter are more than three times the summer levels. This indicates that while PN levels and PM₂.₅ levels exhibit parallel seasonal trends, the changes in PN levels are less pronounced compared to the changes in PM₂.₅ levels across different seasons.

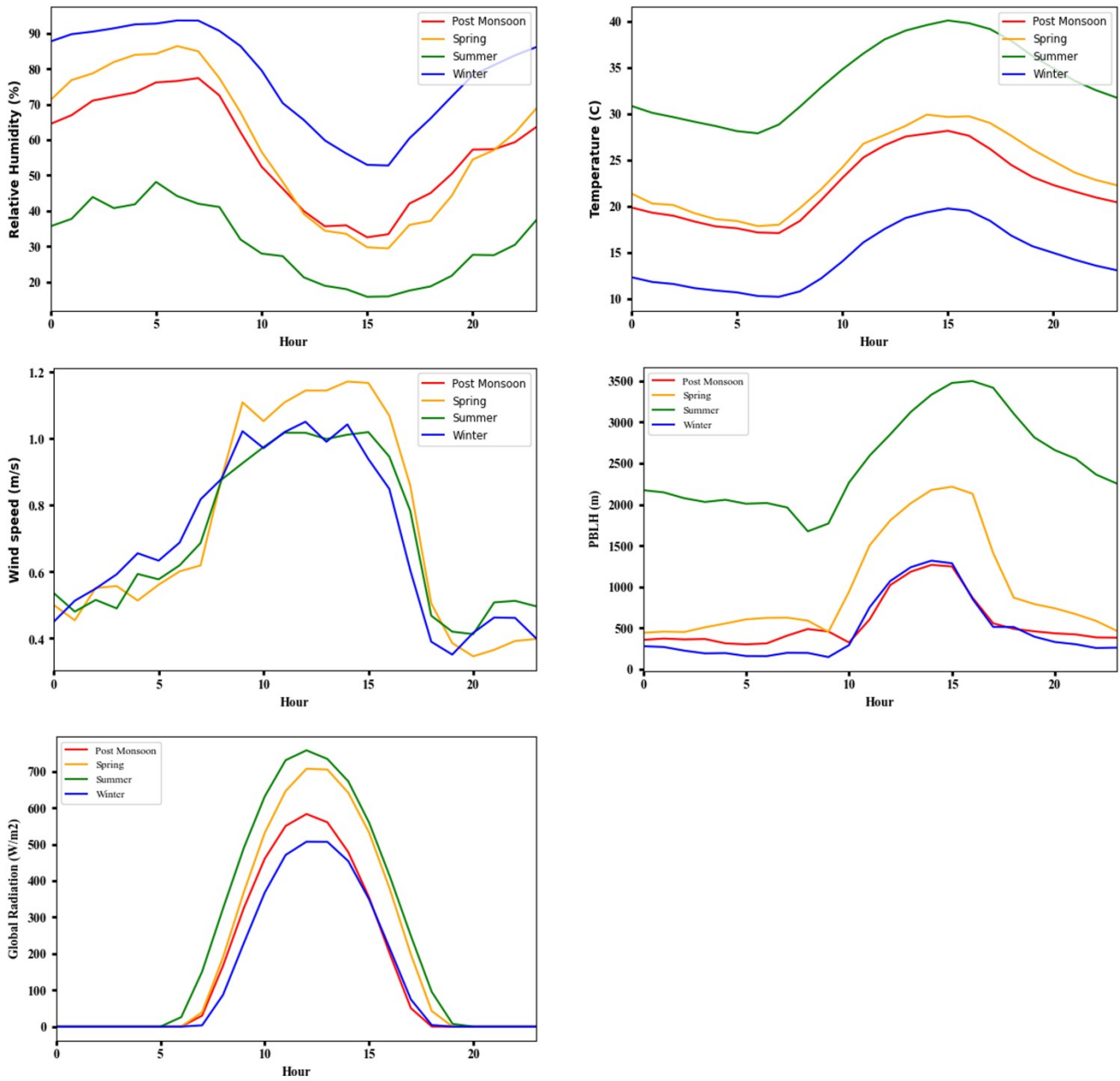296

297

298

299

Figure S10: Diurnal variation of meteorological parameters during different seasons.

300

301

302
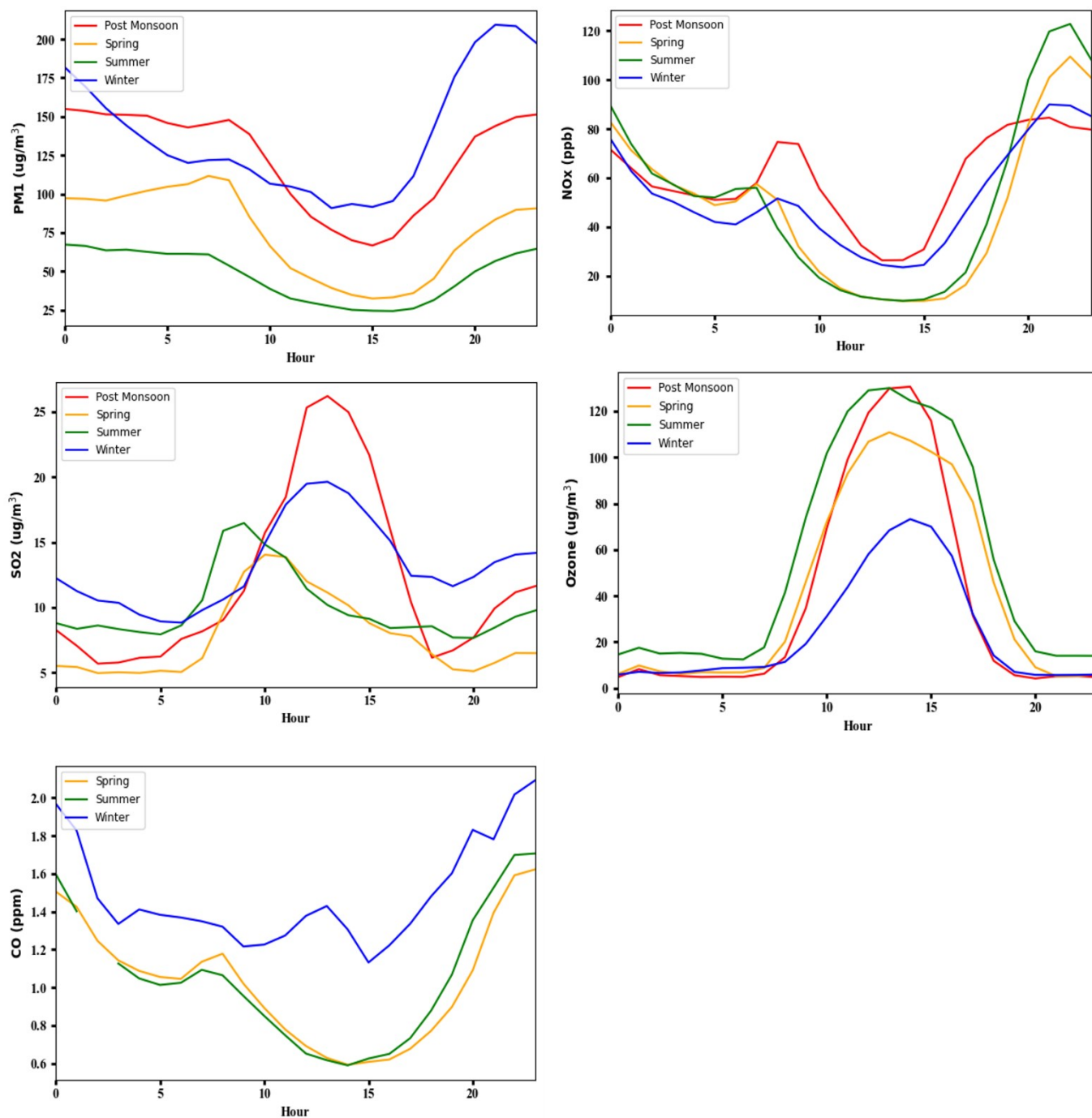
303

304

305

306

307

308

309

Figure S11: Diurnal variation of trace pollutants during different seasons.
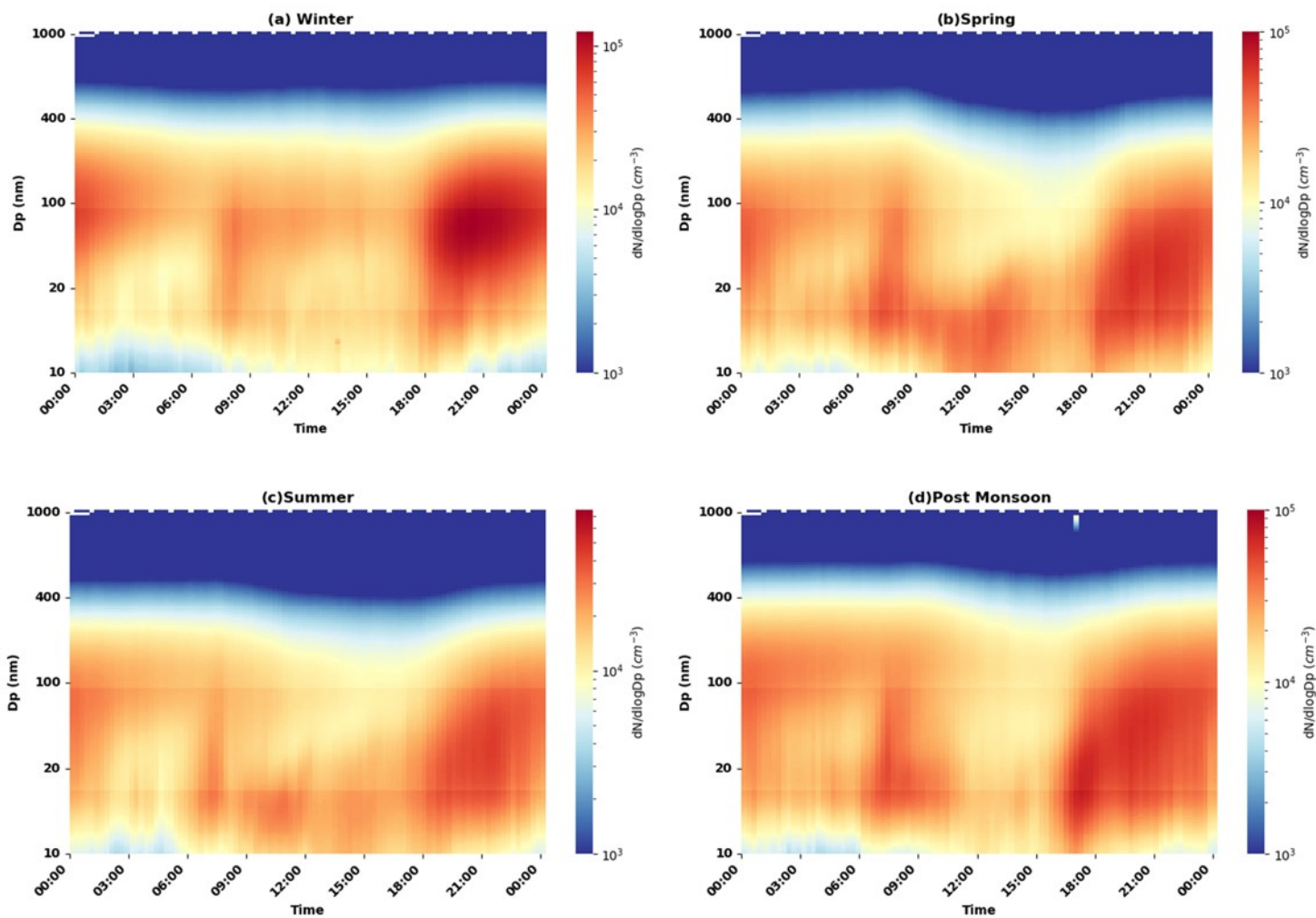
310

311

312

313

314

315

Figure S12: PNSD Heatmaps during different seasons. On y-axis is particle diameter (Dp), on x-axis is time of the day and colour intensity represent particle number concentration.
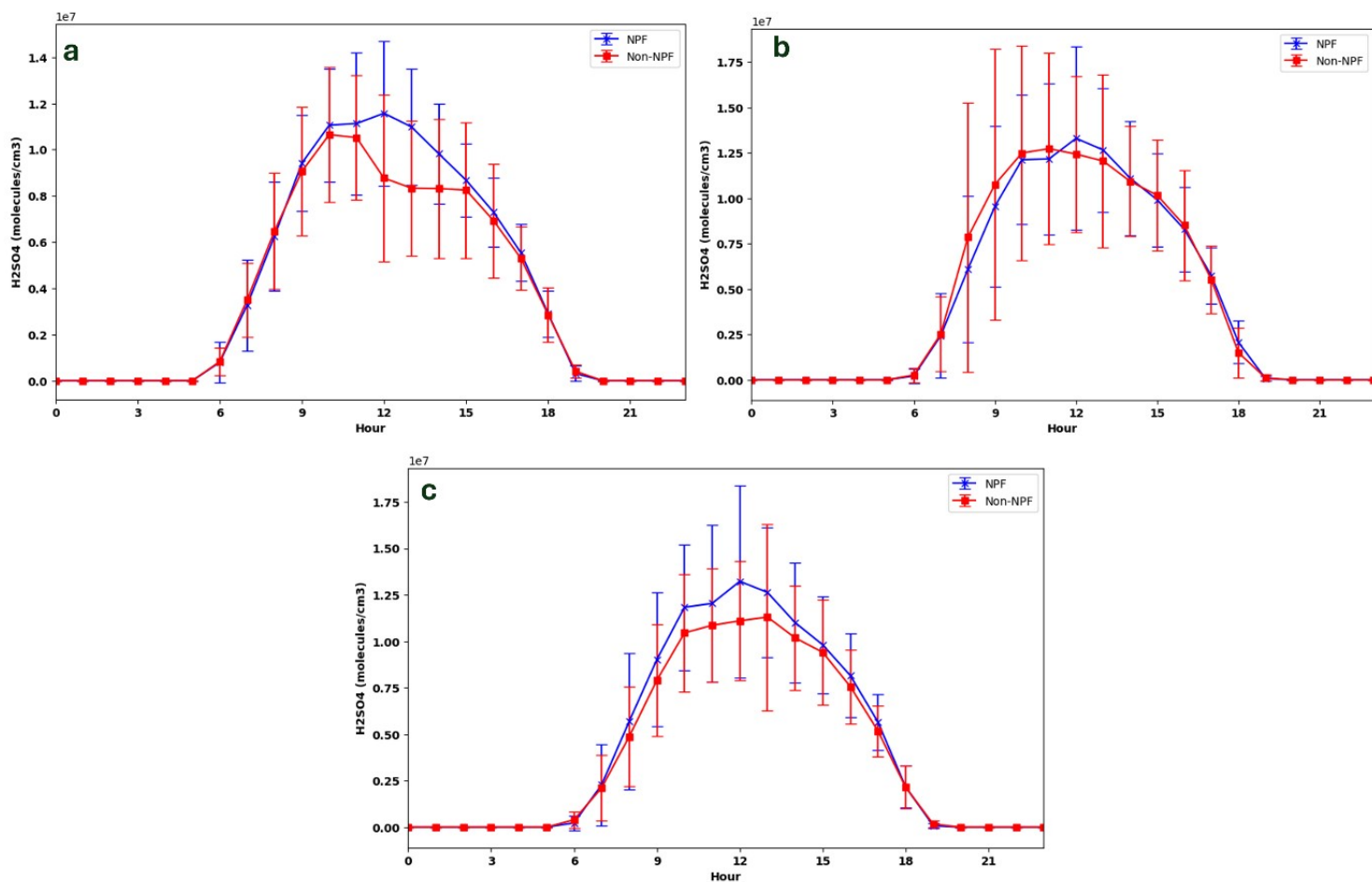
316

317

318

Figure S13:(a and b) Comparison of average daytime hours variation of H_2SO_4 proxy concentration between NPF and non-NPF days during low CS (<0.03 s^{-1}) and medium CS (0.03 to 0.06 s^{-1}); (c) Comparison of average daytime hours variation of H_2SO_4 proxy concentration between NPF and non-NPF days spring and summer seasons only when most of observed our NPF events occurred.
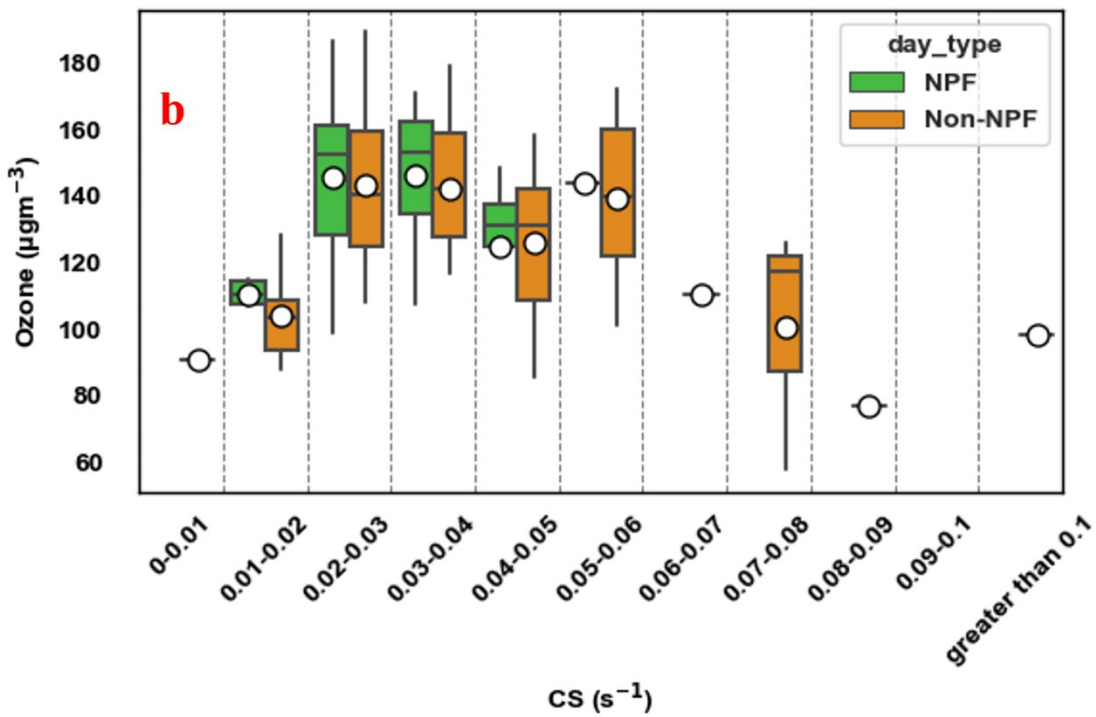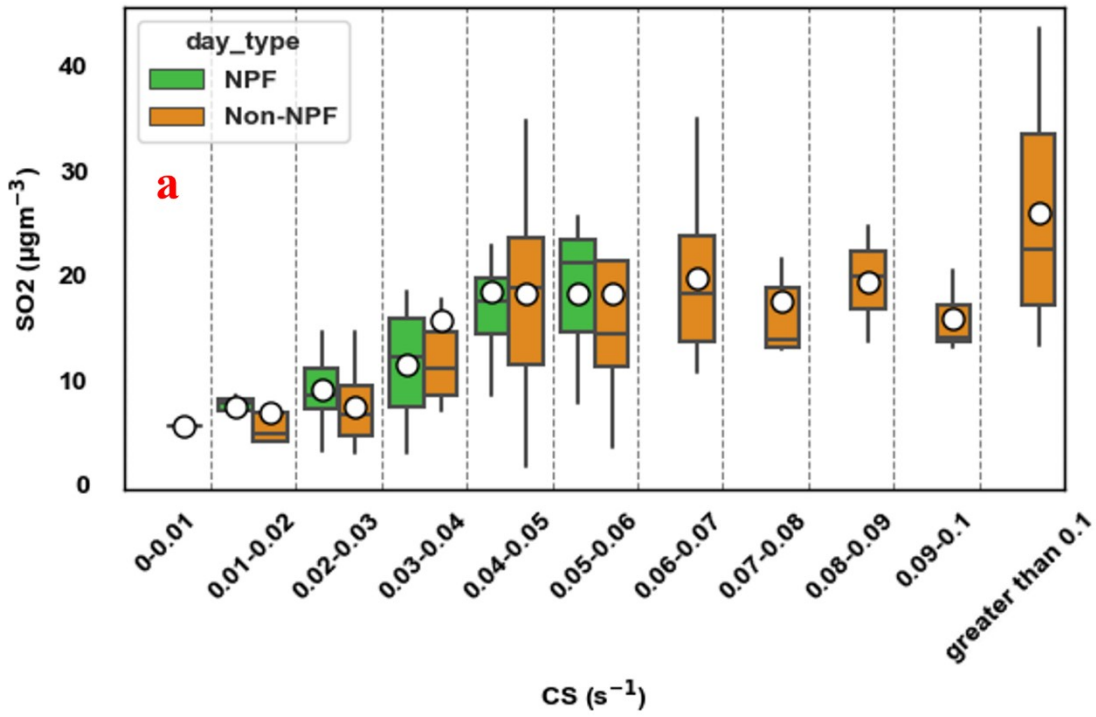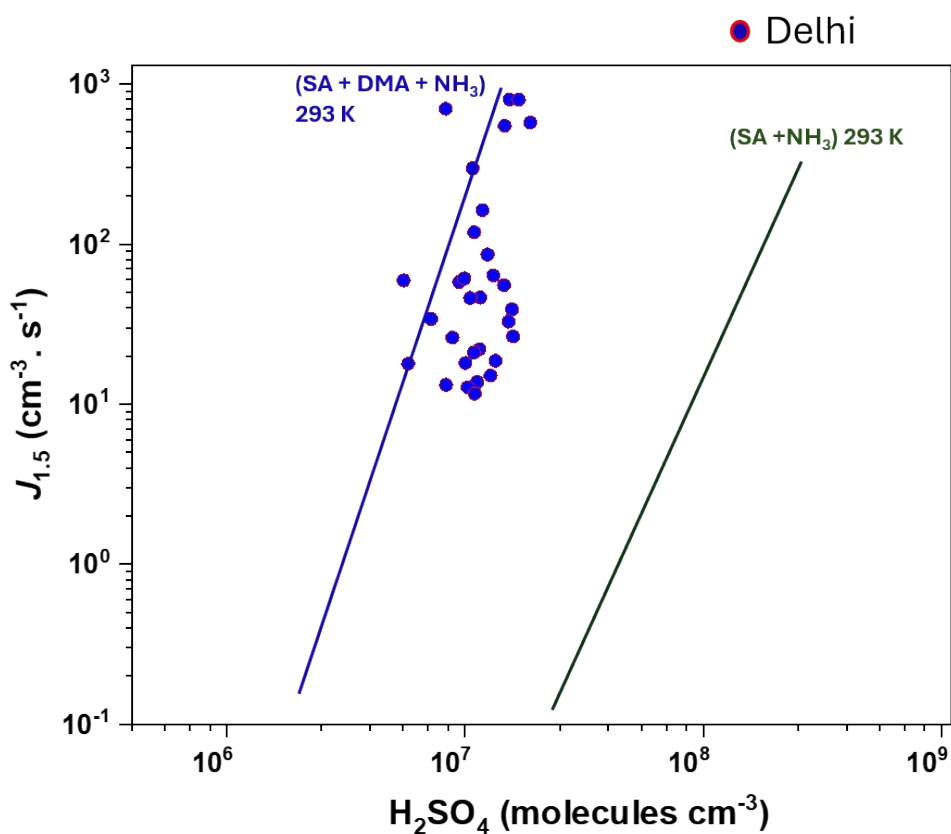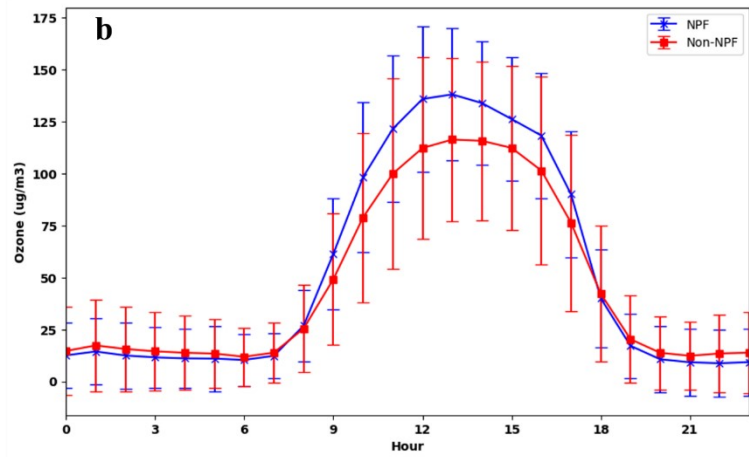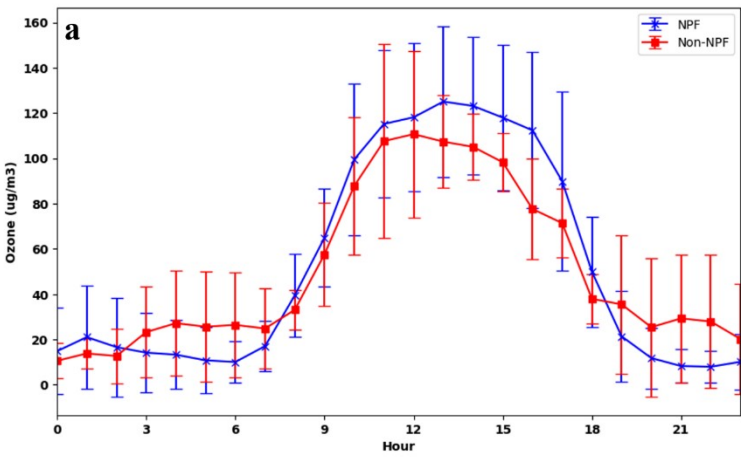
319

320

321

322

Figure S14: (a and b) Average daily variation of SO₂ and Ozone versus CS (s⁻¹). Each data point represents the average of the variable from 10:00 to 16:00 local time (LT).

323

324

Figure S15: The relationship between nucleation rate ($J_{1.5}$) and sulfuric acid concentration [H_2SO_4] under different precursor conditions at 293 K. The blue line represents the nucleation rate for the system with sulfuric acid, dimethylamine (DMA), and ammonia (NH_3), while the green line represents the system with sulfuric acid and ammonia only.

326

Figure S16:(a and b) Comparison of average diurnal variation of measured ozone concentration between NPF and non-NPF days during low CS (<0.03 s^{-1}) and medium CS (0.03 to 0.06 s^{-1}).

327

328

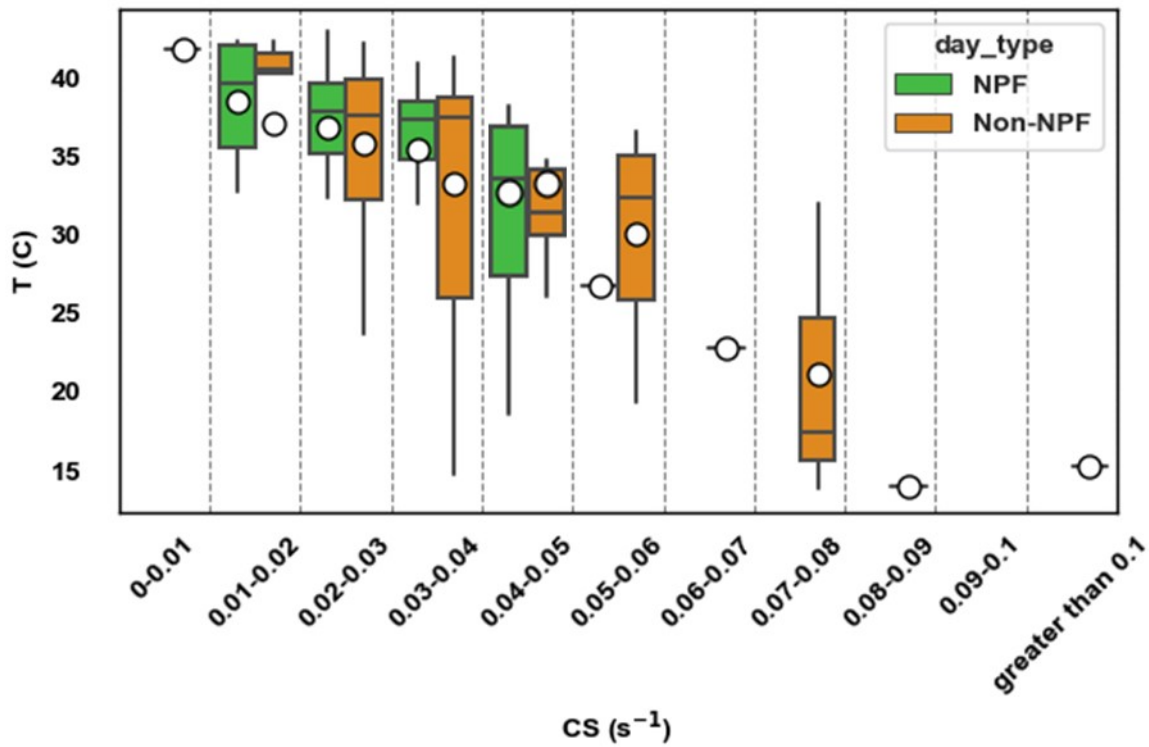*Figure S17: (a and b) Average daily variation of T versus CS (s-1). Each data point represents the average of the variable from 10:00 to 16:00 local time (LT).*
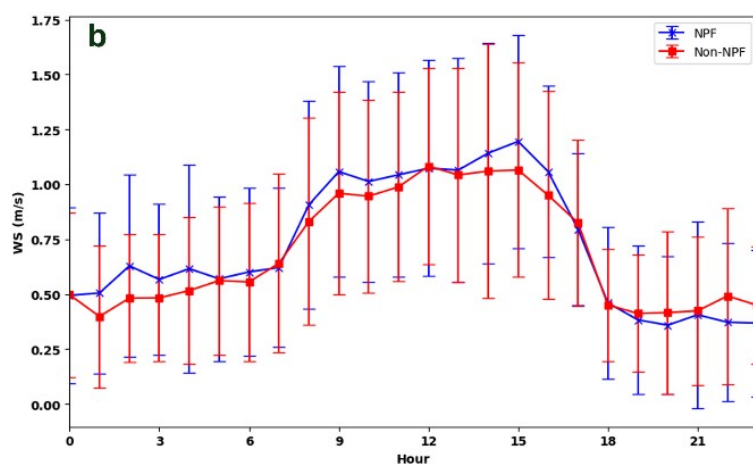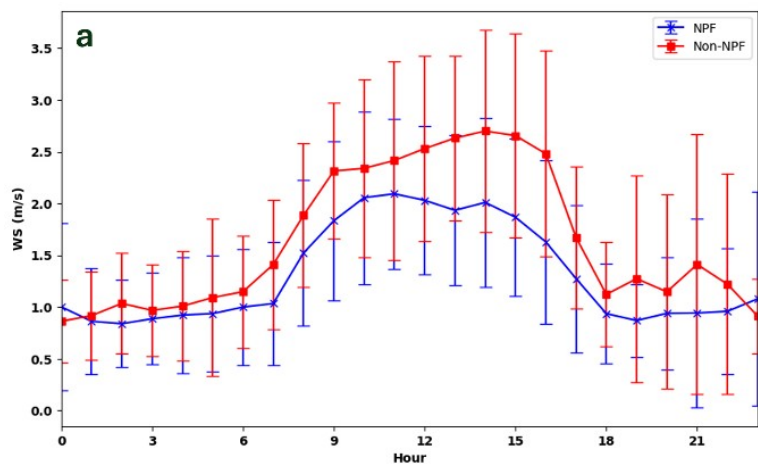
Figure S18:(a and b) Comparison of average diel variation of wind speeds (WS) concentration between NPF and non-NPF days during low CS (<0.03 s⁻¹) and medium CS (0.03 to 0.06 s⁻¹).
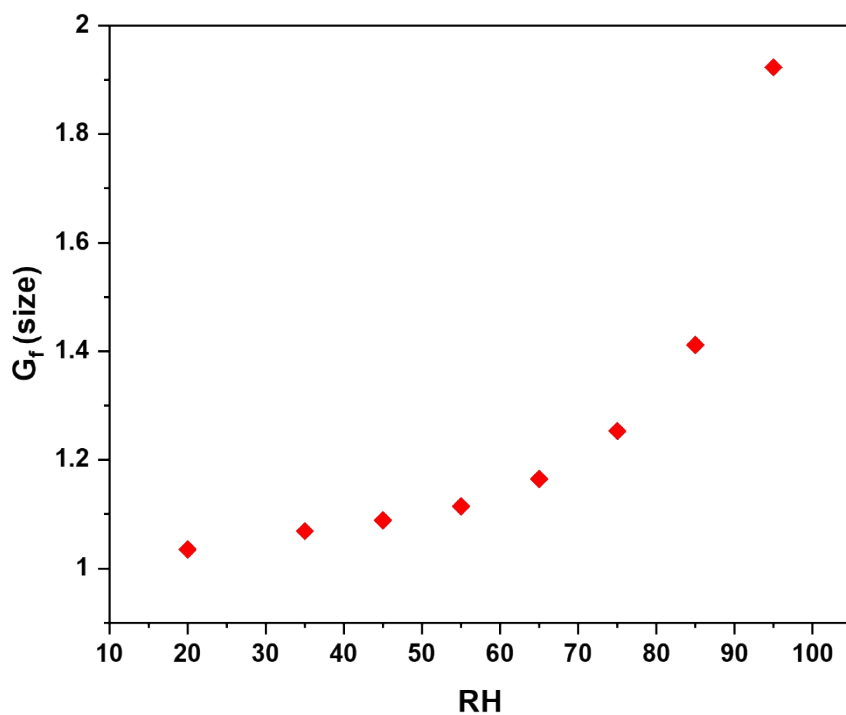
Figure S19: Hygroscopic Growth Factor (Size-Based) (G_f) vs. Relative Humidity (RH, %) :In the RH range of 30-60%, the size enhancement of aerosol particles is between 5-15%. This increase in size directly influences the condensation sink (CS) due to the linear relationship between CS and particle size in the continuum regime.
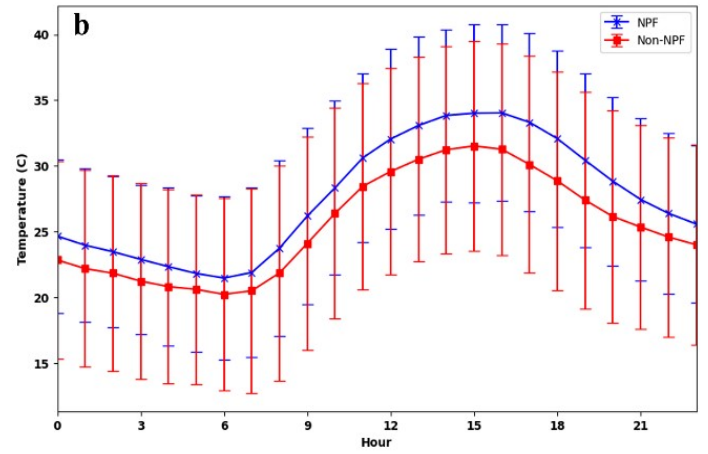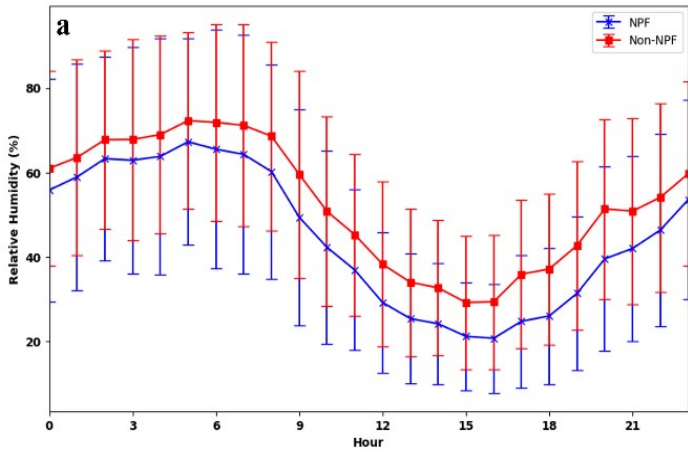
340
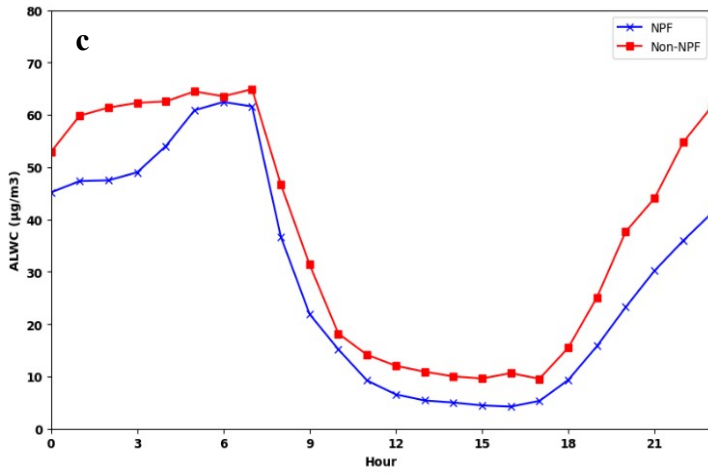
Figure S20: Average diurnal variation of RH, T and ALWC between NPF and non-NPF days during medium CS region (0.03 to 0.06 s⁻¹).

348

349

350

351

352

353

354

355

356

357

358

359
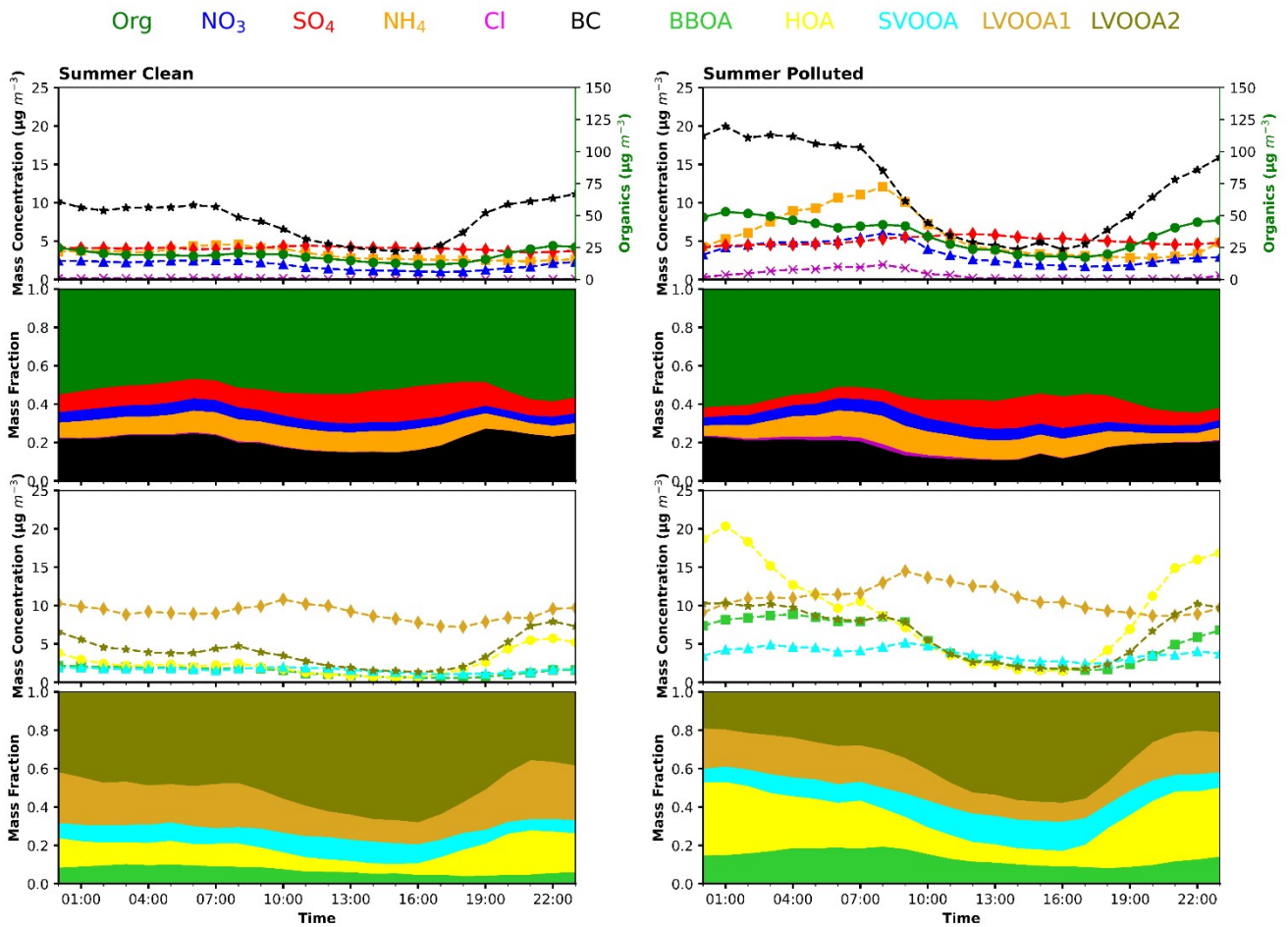
Figure S21: Diurnal variation of average composition of $PM_{2.5}$ during clean and polluted days of summer season. Sulphate and oxygenated organic aerosols (LVOOA2) dominated the mass fractions of inorganics and organics, respectively, during the daytime when observed NPF events take place in our study both clean and polluted periods. The behaviour is similar to spring season, as shown in Figure 7.

360

361

362

363
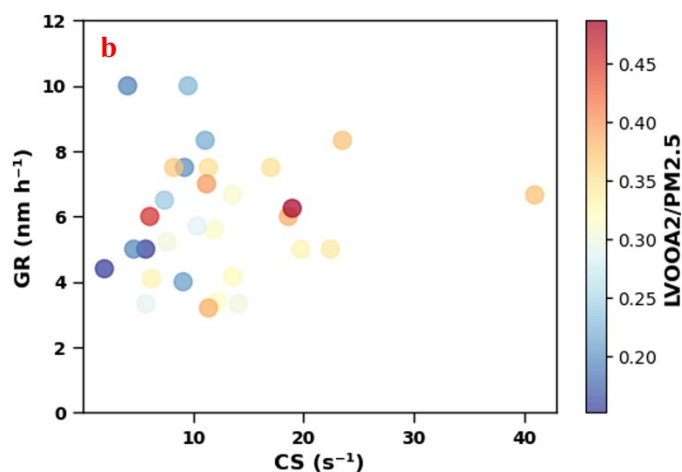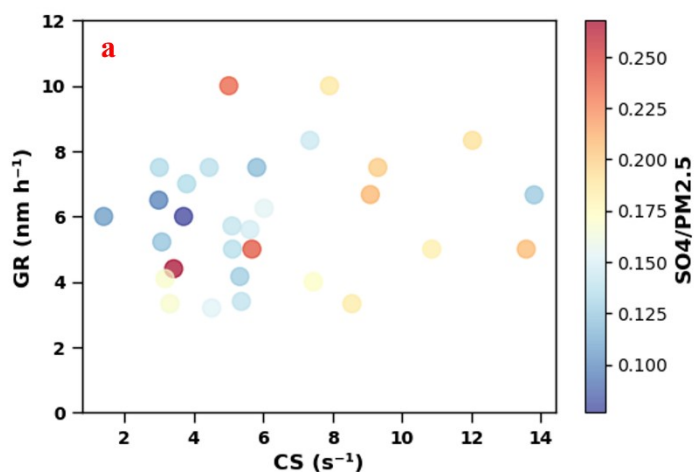
364

Figure S22: (a) the relationship between GR and CS, color-coded by (a) SO4/PM2.5 and (b) LVOOA2/PM2.5. While SO4 and LVOOA2 fractions are at their highest during daytime NPF events and dominate PM2.5, their ratios do not singularly dictate the growth rates of nucleation mode particles. The findings underscore the need for a more comprehensive approach, incorporating a broader range of variables and interactions to understand particle growth dynamics during NPF events fully.

365

366

367

368

369

370

371

372

373

374

375

376

377

378
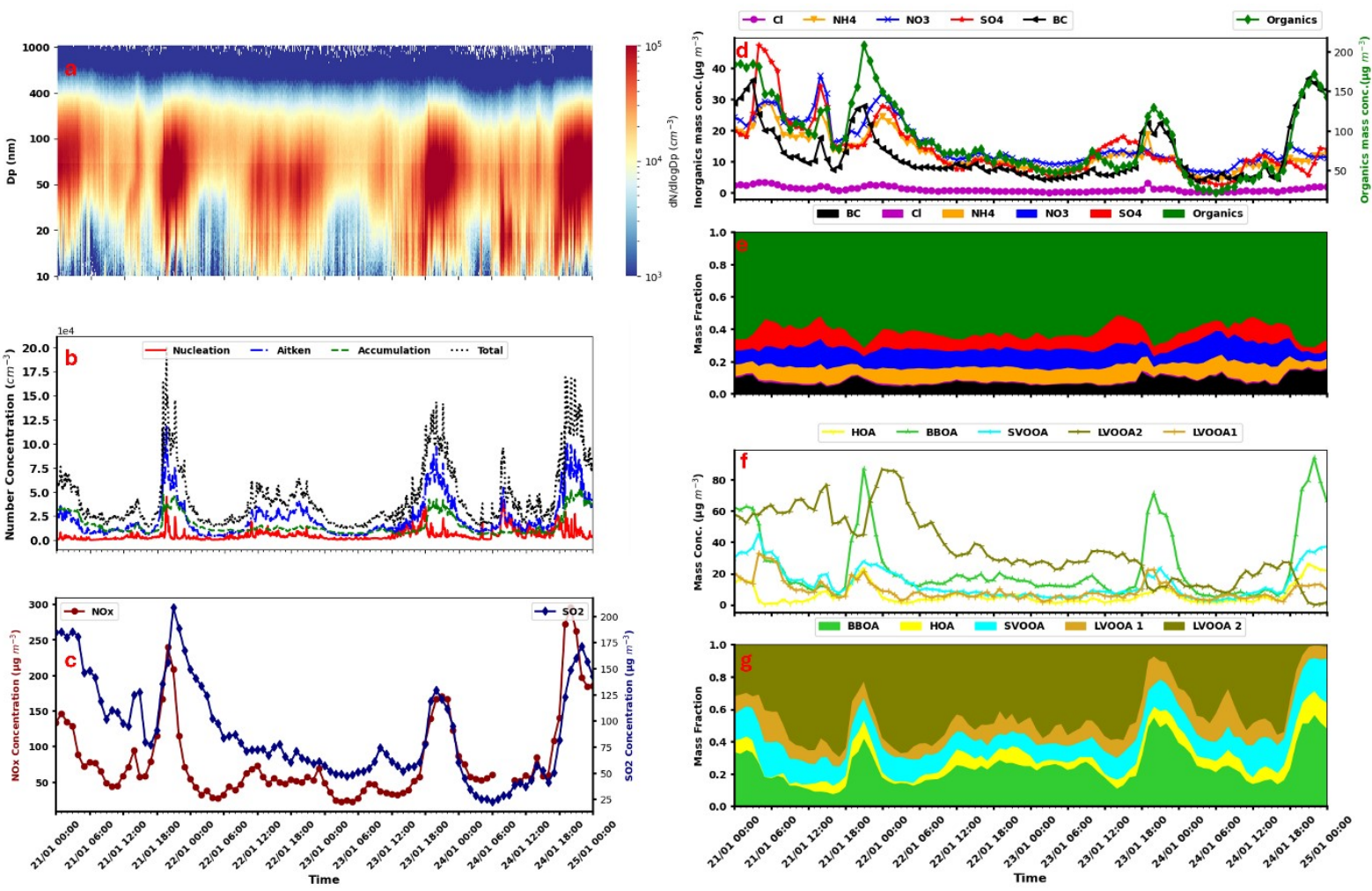
Figure S23: Temporal variation of particle size distribution, mode concentrations, trace gases (NOx and SO₂) along with chemical composition of PM₂.₅ on three consecutive polluted days of winter season. Higher CS inhibited the NPF during daytime. However, primary emitted particles undergo nighttime rapid growth due to coagulation between particles and condensation of vapours resulting from low RH and T. Primary nature of these processes is validated by the increase in mass concentration of

379

380

381

382

383

384

385

386

387

388

389

390

391 1. Chetna, ., Dhaka, S. K., Longiany, G., Panwar, V., Kumar, V., Malik, S., Rao, A. S.,
392   Singh, N., Dimri, A. P., Matsumi, Y., Nakayama, T., & Hayashida, S. (2023). Trends
393   and Variability of PM2.5 at Different Time Scales over Delhi: Long-term Analysis
394   2007–2021. *Aerosol and Air Quality Research*, *23*(5), 220191.
395   https://doi.org/10.4209/aaqr.220191

396 2. Li, J., Hao, X., Liao, H., Hu, J., & Chen, H. (2021). Meteorological Impact on Winter
397   PM2.5 Pollution in Delhi: Present and Future Projection Under a Warming Climate.
398   *Geophysical Research Letters*, *48*(13), e2021GL093722.
399   https://doi.org/https://doi.org/10.1029/2021GL093722

400 3. Pant, P., Shukla, A., Kohl, S. D., Chow, J. C., Watson, J. G., & Harrison, R. M. (2015).
401   Characterization of ambient PM2.5 at a pollution hotspot in New Delhi, India and
402   inference of sources. *Atmospheric Environment*, *109*, 178–189.
403   https://doi.org/https://doi.org/10.1016/j.atmosenv.2015.02.074

404 4. Gani, S., Bhandari, S., Seraj, S., Wang, D. S., Patel, K., Soni, P., Arub, Z., Habib, G.,
405   Hildebrandt Ruiz, L., & Apte, J. S. (2019). Submicron aerosol composition in the
406   world's most polluted megacity: The Delhi Aerosol Supersite study. *Atmospheric*
407   *Chemistry and Physics*, *19*(10), 6843–6859. https://doi.org/10.5194/acp-19-6843-2019

408 5. Dada, L., Paasonen, P., Nieminen, T., Buenrostro Mazon, S., Kontkanen, J., Peräkylä, O.,
409   Lehtipalo, K., Hussein, T., Petäjä, T., Kerminen, V. M., Bäck, J., & Kulmala, M. (2017).
410   Long-term analysis of clear-sky new particle formation events and nonevents in
411   Hyytiälä. *Atmospheric Chemistry and Physics*, *17*(10), 6227–6241.
412   https://doi.org/10.5194/acp-17-6227-2017

413 6. Zhou, Y., Hakala, S., Yan, C., Gao, Y., Yao, X., Chu, B., Chan, T., Kangasluoma, J., Gani,
414   S., Kontkanen, J., Paasonen, P., Liu, Y., Petäjä, T., Kulmala, M., & Dada, L. (2021).
415   Measurement report: New particle formation characteristics at an urban and a mountain
416   station in northern China. *Atmospheric Chemistry and Physics*, *21*(23), 17885–17906.
417   https://doi.org/10.5194/acp-21-17885-2021

418 7. Cai, J., Sulo, J., Gu, Y., Holm, S., Cai, R., Thomas, S., Neuberger, A., Mattsson, F.,
419   Paglione, M., Decesari, S., Rinaldi, M., Yin, R., Aliaga, D., Huang, W., Li, Y.,
420   Gramlich, Y., Ciarelli, G., Quéléver, L., Sarnela, N., … Bianchi, F. (2024). Elucidating
421   the mechanisms of atmospheric new particle formation in the highly polluted Po Valley,
422   Italy. *Atmospheric Chemistry and Physics*, *24*(4), 2423–2441.
423   https://doi.org/10.5194/acp-24-2423-2024

424 8. Du, W., Cai, J., Zheng, F., Yan, C., Zhou, Y., Guo, Y., Chu, B., Yao, L., Heikkinen, L. M.,
425   Fan, X., Wang, Y., Cai, R., Hakala, S., Chan, T., Kontkanen, J., Tuovinen, S., Petäjä, T.,
426   Kangasluoma, J., Bianchi, F., … Kulmala, M. (2022). Influence of Aerosol Chemical
427   Composition on Condensation Sink Efficiency and New Particle Formation in Beijing.

428   *Environmental Science and Technology Letters*.

429   https://doi.org/10.1021/acs.estlett.2c00159

430 9. Brean, J., Beddows, D. C. S., Harrison, R. M., Song, C., Tunved, P., Ström, J., Krejci, R.,
431   Freud, E., Massling, A., Skov, H., Asmi, E., Lupi, A., & Dall'Osto, M. (2023).
432   Collective geographical ecoregions and precursor sources driving Arctic new particle
433   formation. *Atmospheric Chemistry and Physics*, *23*(3), 2183–2198.
434   https://doi.org/10.5194/acp-23-2183-2023

435 10. Lai, S., Qi, X., Huang, X., Lou, S., Chi, X., Chen, L., Liu, C., Liu, Y., Yan, C., Li, M.,
436   Liu, T., Nie, W., Kerminen, V.-M., Petäjä, T., Kulmala, M., & Ding, A. (2024). New
437   particle formation induced by anthropogenic–biogenic interactions on the southeastern
438   Tibetan Plateau. *Atmospheric Chemistry and Physics*, *24*(4), 2535–2553.
439   https://doi.org/10.5194/acp-24-2535-2024

440 11. Mönkkönen, P., Koponen, I. K., Lehtinen, K. E. J., Hämeri, K., Uma, R., & Kulmala, M.
441   (2005). Measurements in a highly polluted Asian mega city: observations of aerosol
442   number size distribution, modal parameters and nucleation events. *Atmospheric*
443   *Chemistry and Physics*, *5*(1), 57–66. https://doi.org/10.5194/acp-5-57-2005

444 12. Xiao, S., Wang, M. Y., Yao, L., Kulmala, M., Zhou, B., Yang, X., Chen, J. M., Wang, D.
445   F., Fu, Q. Y., Worsnop, D. R., & Wang, L. (2015). Strong atmospheric new particle
446   formation in winter in urban Shanghai, China. *Atmospheric Chemistry and Physics*,
447   *15*(4), 1769–1781. https://doi.org/10.5194/acp-15-1769-2015

448 13. Andreae, M. O., Andreae, T. W., Ditas, F., & Pöhlker, C. (2022). Frequent new particle
449   formation at remote sites in the subboreal forest of North America. *Atmospheric*
450   *Chemistry and Physics*, *22*(4), 2487–2505. https://doi.org/10.5194/acp-22-2487-2022

451 14. Kanawade, V. P., Tripathi, S. N., Siingh, D., Gautam, A. S., Srivastava, A. K., Kamra, A.
452   K., Soni, V. K., & Sethi, V. (2014). Observations of new particle formation at two
453   distinct Indian subcontinental urban locations. *Atmospheric Environment*, *96*, 370–379.
454   https://doi.org/https://doi.org/10.1016/j.atmosenv.2014.08.001

455 15. Sebastian, M., Kanawade, V. P., & Pierce, J. R. (2021). Observation of sub-3nm particles
456   and new particle formation at an urban location in India. *Atmospheric Environment*, *256*,
457   118460. https://doi.org/https://doi.org/10.1016/j.atmosenv.2021.118460

458 16. Hussein, T., Martikainen, J., Junninen, H., Sogacheva, L., Wagner, R., Dal Maso, M.,
459   Riipinen, I., Aalto, P. P., & Kulmala, M. (2008). Observation of regional new particle
460   formation in the urban atmosphere. *Tellus, Series B: Chemical and Physical*
461   *Meteorology*, *60*(4), 509–521. https://doi.org/10.1111/j.1600-0889.2008.00365.x

462 17. Dinoi, A., Weinhold, K., Wiedensohler, A., & Contini, D. (2021). Study of new particle
463   formation events in southern Italy. *Atmospheric Environment*, *244*, 117920.
464   https://doi.org/https://doi.org/10.1016/j.atmosenv.2020.117920

465 18. Weiwei Hu Pedro Campuzano-Jost, D. A. D. P. C. M. R. C. J. T. J. D. R. W., & Jimenez,
466   J. L. (2017). Evaluation of the new capture vaporizer for aerosol mass spectrometers
467   (AMS) through field studies of inorganic species. *Aerosol Science and Technology*,
468   *51*(6), 735–754. https://doi.org/10.1080/02786826.2017.1296104

469 19. Crenn, V., Sciare, J., Croteau, P. L., Verlhac, S., Fröhlich, R., Belis, C. A., Aas, W.,
470   Äijälä, M., Alastuey, A., Artiñano, B., Baisnée, D., Bonnaire, N., Bressi, M.,
471   Canagaratna, M., Canonaco, F., Carbone, C., Cavalli, F., Coz, E., Cubison, M. J., …
472   Favez, O. (2015). ACTRIS ACSM intercomparison – Part 1: Reproducibility of
473   concentration and fragment results from 13 individual Quadrupole Aerosol Chemical
474   Speciation Monitors (Q-ACSM) and consistency with co-located instruments.
475   *Atmospheric Measurement Techniques*, *8*(12), 5063–5087. https://doi.org/10.5194/amt-
476   8-5063-2015

477 20. Pich, J. (1972). Theory of gravitational deposition of particles from laminar flows in
478   channels. *Journal of Aerosol Science*, *3*(5), 351–361.
479   https://doi.org/https://doi.org/10.1016/0021-8502(72)90090-0

480 21. Ingham, D. B. (1975). Diffusion of aerosols from a stream flowing through a cylindrical
481   tube. *Journal of Aerosol Science*, *6*(2), 125–132.
482   https://doi.org/https://doi.org/10.1016/0021-8502(75)90005-1

483 22. Hu, M., Peng, J., Sun, K., Yue, D., Guo, S., Wiedensohler, A., & Wu, Z. (2012).
484   Estimation of size-resolved ambient particle density based on the measurement of
485   aerosol number, mass, and chemical size distributions in the winter in Beijing.
486   *Environmental Science and Technology*, *46*(18), 9941–9947.
487   https://doi.org/10.1021/es204073t

488 23. Sarangi, B., Aggarwal, S. G., Sinha, D., & Gupta, P. K. (2016). Aerosol effective density
489   measurement using scanning mobility particle sizer and quartz crystal microbalance with
490   the estimation of involved uncertainty. *Atmospheric Measurement Techniques*, *9*(3),
491   859–875. https://doi.org/10.5194/amt-9-859-2016

492 24. Gani, S., Bhandari, S., Patel, K., Seraj, S., Soni, P., Arub, Z., Habib, G., Hildebrandt
493   Ruiz, L., & Apte, J. S. (2020). Particle number concentrations and size distribution in a
494   polluted megacity: the Delhi Aerosol Supersite study. *Atmospheric Chemistry and
495   Physics*, *20*(14), 8533–8549. https://doi.org/10.5194/acp-20-8533-2020

496 25. Laakso, L., Koponen, I. K., Mönkkönen, P., Kulmala, M., Kerminen, V. M., Wehner, B.,
497   Wiedensohler, A., Wu, Z., & Hu, M. (2006). Aerosol particles in the developing world;
498   A comparison between New Delhi in India and Beijing in China. *Water, Air, and Soil
499   Pollution*, *173*(1–4), 5–20. https://doi.org/10.1007/s11270-005-9018-5

500 26. Stokes, R. H., & Robinson, R. A. (1966). Interactions in Aqueous Nonelectrolyte
501   Solutions. I. Solute-Solvent Equilibria. *The Journal of Physical Chemistry*, *70*(7), 2126–
502   2131. https://doi.org/10.1021/j100879a010

503 27. Ali, U., Faisal, M., Ganguly, D., Kumar, M., & Singh, V. (2023). Analysis of aerosol
504   liquid water content and its role in visibility reduction in Delhi. *Science of the Total*
505   *Environment*, *867*. https://doi.org/10.1016/j.scitotenv.2023.161484

506 28. Alfarra, M. R., Prevot, A. S. H., Szidat, S., Sandradewi, J., Weimer, S., Lanz, V. A.,
507   Schreiber, D., Mohr, M., & Baltensperger, U. (2007). Identification of the Mass Spectral
508   Signature of Organic Aerosols from Wood Burning Emissions. *Environmental Science*
509   *& Technology*, *41*(16), 5770–5777. https://doi.org/10.1021/es062289b

510 29. Aiken, A. C., Salcedo, D., Cubison, M. J., Huffman, J. A., DeCarlo, P. F., Ulbrich, I. M.,
511   Docherty, K. S., Sueper, D., Kimmel, J. R., Worsnop, D. R., Trimborn, A., Northway,
512   M., Stone, E. A., Schauer, J. J., Volkamer, R. M., Fortner, E., de Foy, B., Wang, J.,
513   Laskin, A., … Jimenez, J. L. (2009). Mexico City aerosol analysis during MILAGRO
514   using high resolution aerosol mass spectrometry at the urban supersite (T0) – Part 1:
515   Fine particle composition and organic source apportionment. *Atmospheric Chemistry*
516   *and Physics*, *9*(17), 6633–6653. https://doi.org/10.5194/acp-9-6633-2009

517 30. N. L. Ng S. C. Herndon, A. T. M. R. C. P. L. C. T. B. O. D. S. D. R. W. Q. Z. Y. L. S., &
518   Jayne, J. T. (2011). An Aerosol Chemical Speciation Monitor (ACSM) for Routine
519   Monitoring of the Composition and Mass Concentrations of Ambient Aerosol. *Aerosol*
520   *Science and Technology*, *45*(7), 780–794.
521   https://doi.org/10.1080/02786826.2011.560211

522 31. Zimmerman, A., Petters, M. D., & Meskhidze, N. (2020). Observations of new particle
523   formation, modal growth rates, and direct emissions of sub-10 nm particles in an urban
524   environment. *Atmospheric Environment*, *242*, 117835.
525   https://doi.org/https://doi.org/10.1016/j.atmosenv.2020.117835

526 32. Kulmala, N. (2016). *On the mode-segregated aerosol particle number concentration*
527   *load : contributions of primary and secondary particles in.*
528   http://hdl.handle.net/10138/165340

529 33. Pey, J., Querol, X., Alastuey, A., Rodríguez, S., Putaud, J. P., & Van Dingenen, R.
530   (2009). Source apportionment of urban fine and ultra-fine particle number concentration
531   in a Western Mediterranean city. *Atmospheric Environment*, *43*(29), 4407–4415.
532   https://doi.org/https://doi.org/10.1016/j.atmosenv.2009.05.024

533 34. Kulmala, M., Petäjä, T., Nieminen, T., Sipilä, M., Manninen, H. E., Lehtipalo, K., Dal
534   Maso, M., Aalto, P. P., Junninen, H., Paasonen, P., Riipinen, I., Lehtinen, K. E. J.,
535   Laaksonen, A., & Kerminen, V. M. (2012). Measurement of the nucleation of
536   atmospheric aerosol particles. *Nature Protocols*, *7*(9), 1651–1667.
537   https://doi.org/10.1038/nprot.2012.091

538 35. KULMALA, M., MASO, M. D., MAKELA, J. M., PIRJOLA, L., VAKEVA, M.,
539   AALTO, P., MIIKKULAINEN, P., HAMERI, K., & O'DOWD, C. D. (2001). On the
540   formation, growth and composition of nucleation mode particles. *Tellus B*, *53*(4), 479–
541   490. https://doi.org/10.1034/j.1600-0889.2001.530411.x

542   36. *ATMOSPHERIC CHEMISTRY AND PHYSICS*. (n.d.).

543   37. Dada, L., Ylivinkka, I., Baalbaki, R., Li, C., Guo, Y., Yan, C., Yao, L., Sarnela, N.,
544   Jokinen, T., Daellenbach, K. R., Yin, R., Deng, C., Chu, B., Nieminen, T., Wang, Y.,
545   Lin, Z., Thakur, R. C., Kontkanen, J., Stolzenburg, D., … Kulmala, M. (2020). Sources
546   and sinks driving sulfuric acid concentrations in contrasting environments: implications
547   on proxy calculations. *Atmospheric Chemistry and Physics*, *20*(20), 11747–11766.
548   https://doi.org/10.5194/acp-20-11747-2020

549   38. Mikkonen, S., Romakkaniemi, S., Smith, J. N., Korhonen, H., Petäjä, T., Plass-Duelmer,
550   C., Boy, M., McMurry, P. H., Lehtinen, K. E. J., Joutsensaari, J., Hamed, A., Mauldin
551   III, R. L., Birmili, W., Spindler, G., Arnold, F., Kulmala, M., & Laaksonen, A. (2011).
552   A statistical proxy for sulphuric acid concentration. *Atmospheric Chemistry and Physics*,
553   *11*(21), 11319–11334. https://doi.org/10.5194/acp-11-11319-2011

554   39. Petäjä, T., Mauldin III, R. L., Kosciuch, E., McGrath, J., Nieminen, T., Paasonen, P.,
555   Boy, M., Adamov, A., Kotiaho, T., & Kulmala, M. (2009). Sulfuric acid and OH
556   concentrations in a boreal forest site. *Atmospheric Chemistry and Physics*, *9*(19), 7435–
557   7448. https://doi.org/10.5194/acp-9-7435-2009

558

559

560